FACULDADE DE ENGENHARIA DA UNIVERSIDADE DO PORTO

Processing and integrating handheld 3D optical sensor scanning data in an industrial environment

Ricardo Wang

WORKING VERSION

Mestrado Integrado em Engenharia Eletrotécnica e de Computadores

Supervisor: Dr. Roger Groves

Second Supervisor: Dr. Michaël Maria

Third Supervisor: Dr. Miguel Velhote Correia

October 26, 2021

Abstract

The field of non-destructive testing of materials is constantly evolving, allowing researchers and engineers to solve problems in many scientific and industrial fields. Various techniques and methods have been developed such as Ultrasonic Testing, Radiographic Testing or Electromagnetic Testing. Optical coherence tomography (OCT) is a promising imaging technique, offering a great capability of non-invasive, cross-sectional, in vivo, high resolution and three-dimensional tomographic imaging. As a non-destructive testing technique, optical coherence tomography has better spatial resolution than ultrasonic testing and better depth penetration and a larger scan area than microscopy. However, the lateral field of view (FOV) of OCT is extremely limited, deterring the macroscopic examination of surface areas. In this dissertation, this issue was tackled, and a multi-volume registration algorithm was developed to stitch multiple OCT volumes and generate a 3D volume of the scanned area. Using a rotational stage is possible to scan an object with a circular geometry from multiple angles and get a complete notion of the totality of its volume. First, we acquired a dataset with multiple overlapping OCT volumes. Then, image pre-processing techniques were used to denoise and prepare the volumes and images for the registration process. After, image registration methods were used to estimate the translation between consecutive volumes. Finally, after stitching all volumes together, one single volume was successfully generated.

Contents

List of Figures

List of Tables

Abbreviations and Symbols

OCT	Optical Coherence Tomography
FOV	Field Of View
TD-OCT	Time-Domain OCT
FD-OCT	Fourier-Domain OCT
SD-OCT	Spectral-Domain OCT
SS-OCT	Swept-Source OCT

Chapter 1

Introduction

Non-destructive testing (NDT) consists of a variety of methods to evaluate the properties of a material, component, structure or system without damaging it or destroying its serviceability [9]. This assessment is mainly focused on the material integrity for surface or internal flaws or the discontinuities and differences in material characteristics. The field of non-destructive testing of materials is constantly evolving, allowing researchers and engineers to solve problems in many scientific and industrial fields. Today modern non-destructive tests are used in manufacturing and are integral part of the oil and gas and petrochemical industries, along with several other industries, including chemicals, aerospace, military and defense, and automotive [10].

A wide range of techniques and approaches are used in the NDT field, the most common being Visual Testing, Ultrasonic Testing, Radiographic Testing, Electromagnetic Testing, Magnetic Particle Testing, Liquid Penetrant Testing, Leak Testing and Acoustic Emission Testing [11]. However, applications like examination of artworks or objects composed of thin layers [12] require a fast, contactless, non-invasive, and high-resolution imaging of subsurface features at the micrometer range, which is still very limited [13]. When selecting an optical non-destructive technique for imaging of subsurface features, both spatial and depth resolution will have to be considered, as well as the light penetration [14].

One technology that meets all these requirements is optical coherence tomography (OCT). OCT is a purely optical, non-destructive, non-invasive, and contactless high resolution imaging method, allowing the acquisition of one up to three spatial dimensional depth resolved image data of sub-surface regions in real time for in-situ process feedback. Depending on the material, penetration depths of several millimeters can be achieved, thus providing an attractive solution that can be used both as a stand-alone and as a process-integrated solution [15]. As a non-destructive testing technique, optical coherence tomography has better spatial resolution than ultrasonic testing and better depth penetration than microscopy. A sample OCT image can be seen in Figure 1.1.

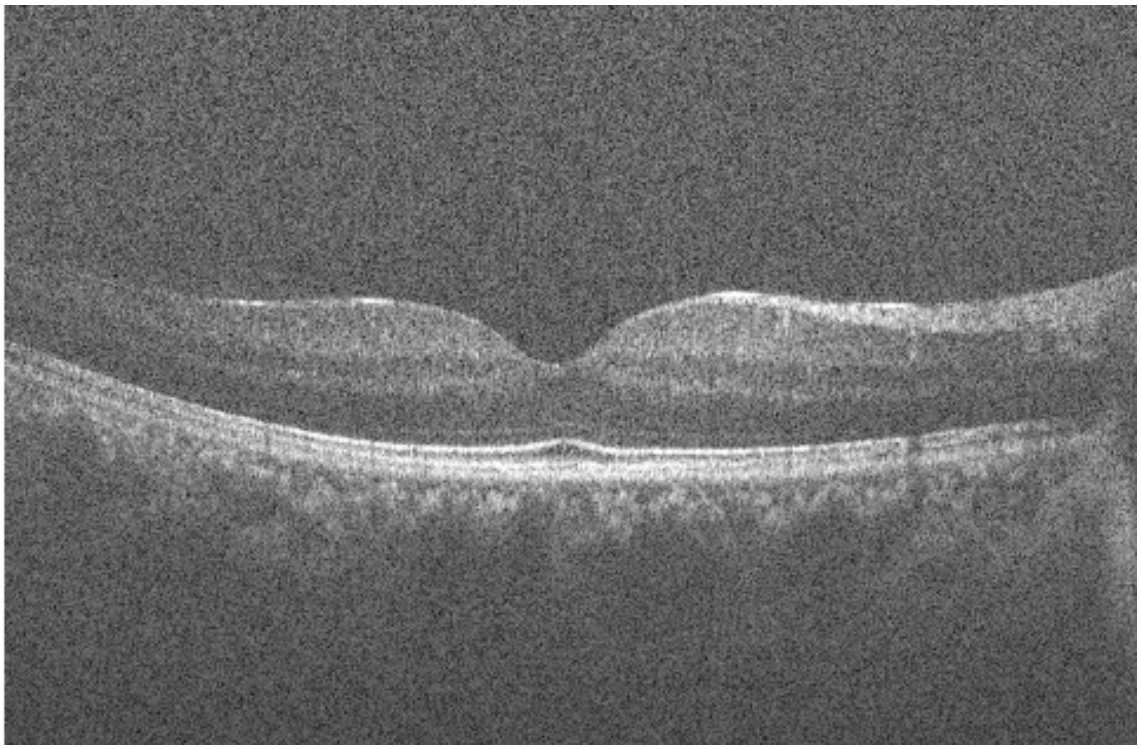

Figure 1.1: Sample OCT image [1]

1.1 Overview and Research Aims

Current optical coherence tomography (OCT) imaging systems are impaired with a relatively short ranging distance and small field of view (FOV). Such narrow FOV can be a key impediment to many possible applications for this technology, where a more complete notion of the imaging structure is needed. Therefore, with the aim of expanding further in vivo OCT applications, there has been a rising interest in seeking solutions to these limitations.

The goal of this dissertation is to develop a 3D reconstruction algorithm capable of stitching multiple OCT volumes in order to increase the field of view (FOV) of this imaging method, making it a viable tool in an industrial environment for non-destructive testing purposes. Since the problem at hand is the imaging of an object with a circular symmetry, using a rotational stage and/or it is possible to scan the whole object from multiple angles, allowing a macro understanding of the whole imaging surface. The OCT volumes give surface and subsurface information that can be useful for the analysis of the imaging surface.

During the first phase of the project, we had to get familiarized and setup the OCT system with the rotational stage and the robotic arm, while also programming the respective control software. Then, after establishing the communication between the different components, we acquired a dataset of overlapping OCT volumes by imaging adjacent volumes of an circular object. Then, we applied image pre-processing techniques such as image smoothing and morphological operations to remove the inherent noise present in the OCT volumes in order to enable the registration process. After, we used image registration methods to estimate the translation between adjacent

volumes, namely template matching. Finally, after stitching all volumes together, we successfully obtained one single volume. In the end, the display of OCT data was greatly improved, allowing a better assessment of the properties of the structure in question.

1.2 Related work

Numerous 3D OCT registration algorithms have been proposed in the literature. The majority of the research on registration of 3D OCT is directed on the 2D registration of planar projections of volumes. One paper presented a multi-tile registration algorithm based on phase correlation to determine the translation among all image pairs [16]. Registration of medical OCT en face fundus images (images that provide an en-face view of any given layer within the volume) was also successfully achieved by utilizing blood vessel ridges as distinguishable features. Stitching of volumetric OCT data was accomplished by using external navigation data and further microscopic images [17]. A novel algorithm performs the stitching of multiple 3D OCT overlapping volumes by utilizing dense volumetric pixels (voxel) information in the registration procedure. Another work performed rigid registration OCT volumes using a 3D extension of the well known 2D SIFT feature detector. Later, this method was improved to have an additional depth alignment [18].

1.3 Main contributions

This dissertation proposes an efficient and accurate registration method for OCT volumes. The major contributions of this thesis are:

- The setup and control of the complete imaging system.
- The acquisition of a dataset with overlapping OCT volumes.
- The presentation of a novel method to register multiple 3D OCT volumes using image pre-processing, denoising and template matching techniques.
- The robustness of the method is displayed on OCT volumes acquired in an industrial environment

1.4 Outline of Dissertation

In addition to this chapter, the organization of the thesis is as follows. Chapter 2 provides a solid introduction to optical coherence tomography and its principles, then presents its main two methodologies and some of its challenges. Chapter 3 introduces image pre-processing techniques used to filter and denoise an image. Chapter 4 explains the image stitching process and some of the most important methods. Chapter 5 describes the OCT imaging system and the remaining hardware used in our experiments, and respective control software. Chapter 6 proposes a framework

of an automated stitching algorithm for Wide Field-of-View OCT and presents our experimental results. Chapter 7 draws some concluding remarks and explores future endeavors.

Chapter 2

Optical coherence tomography

2.1 Introduction to optical coherence tomography

Optical coherence tomography (OCT) is an emerging non-invasive, high-resolution optical imaging modality [12]. As other tomographic techniques, it generates cross-sectional images or slices through a three-dimensional object. Initially applied to the medical field [19], it distinguished itself by generating depth-resolved tomographic images in real time for in-situ process feedback, by extracting information of optical scattering from subsurface regions. Depending on the material, penetration depths of several millimeters can be achieved, thus providing an attractive solution that can be used both as a stand-alone and as a process-integrated solution [15].

In comparison to other 3D imaging modalities, OCT fulfills a space between optical confocal microscopy and ultrasound imaging, having better depth penetration and a larger scan area than the former and a better spatial resolution than the later. Current OCT technologies have axial resolutions ranging from 1 to 15 m, approximately 10–100 times finer than standard ultrasound imaging [20], while being able to reach higher penetration depths 1-3mm compared to only 250µm provided by the confocal microscopy devices [21, 22]. A comparison between these imaging methods by their resolutions and penetration depths in tissues is shown in Figure 2.1.

Abundant innovation and rich technology advancements achieved in the last few years regarding interference technologies, optical instruments,light sources along with faster data acquisition and processing methods have extended the application of OCT systems in a variety of medical fields such as dermatology, ophthalmology and cardiology [23]. In addition, OCT technology is also being applied in other fields, especially in the field of industrial measurement as well as artwork examination and restoration [24].

2.1.1 Principles of optical coherence tomography

Optical coherence tomography can be correlated to ultrasound imaging because of the analogous working principles. An ultrasound scanner generates ultrasound waves, directing them to the imaging sample, and measures the magnitude and traveling time of returning echoes [25]. This

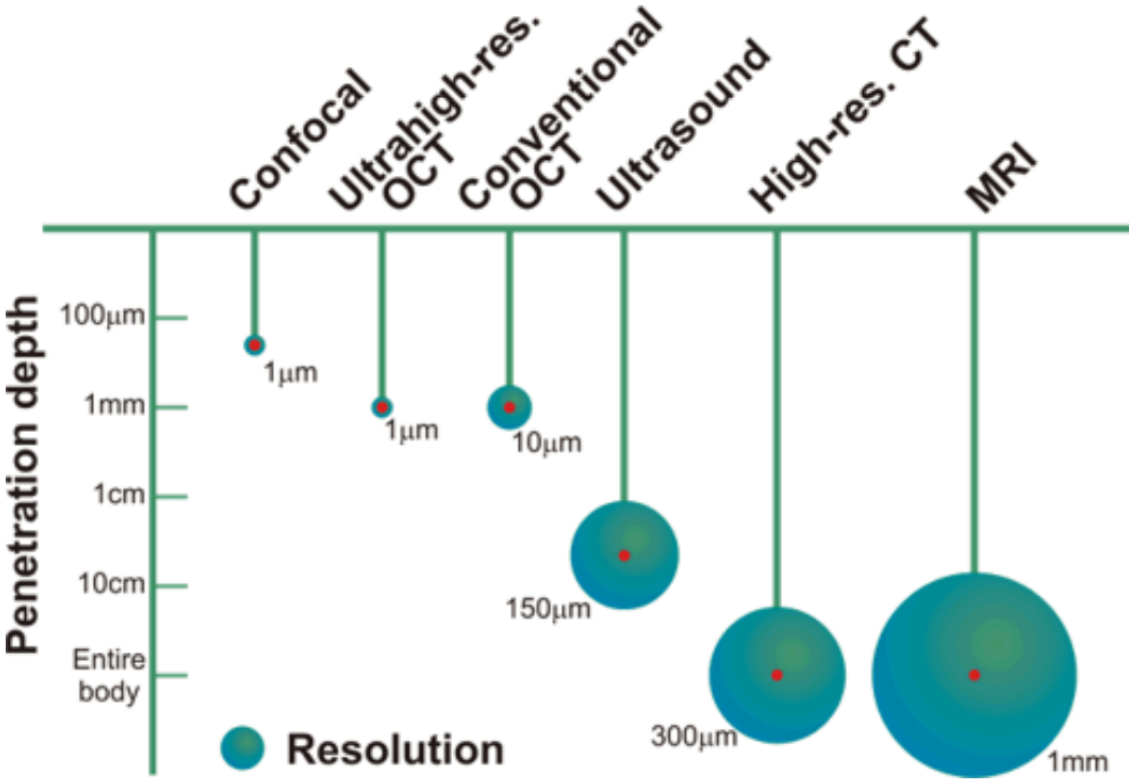

Figure 2.1: Comparison of image resolution and depth of penetration between OCT and other image modalities [2]

analysis of the back reflected waves and respective delay indicates the depth in which the reflection occurred, creating ultrasound images. OCT implements a comparable pulse-echo imaging principle but utilizes light instead of sound waves, as an information medium. Nonetheless, since light travels much faster than sound it is difficult to measure the delays of the back reflected waves directly. Thus, OCT uses low-coherence interferometry to evaluate the returning optical echoes and travelling time with high sensitivity [26].

Making use of an interferometer, the light is split into two light beams, with one being directed to the sample and the other being sent to a reference arm, with known light path length and time delay. A subsequent combination of the returning echoes from both paths occurs at the interferometer output [21]. There, in certain circumstances, interference may be observed, being stronger when the reference and sample path lengths differ by less than the coherence length, which is the propagation distance over which a coherent light wave maintains a specific degree of coherence [20]. Therefore, to acquire images with high axial resolution the path length differences have to be minimal and a low-coherence light source, with a broad bandwidth of light spectrum, is required in OCT. Following the measurement of the interference, is possible to compute the magnitude and time delay of the optical waves by implementing signal demodulation methods.

A generic OCT system schematic is illustrated in Figure 2.2 [3]. Light from a low-coherence source is directed into a simple Michelson interferometer, implemented using a 2×2 fiber–optic

coupler, where the incident optical power is split into reference and sample arms. In the first arm, the light is reflected by a mirror, where in the second arm, the light is focused on the sample through different objective lenses to scan the desired spot [21]. Then, the back-scattered light echoes from the sample are redirected back into the corresponding fiber and recombined at the coupler with the returning reference arm [3], generating an interference pattern, which is recorded by the detector [2]. The detector will measure the intensity of the resulting interfering beams, and then the resulting signal is sent to the signal processing unit [21]. For each sample point, a complete depth reflectivity profile is obtained, generating a A-scan [27]. Moving the focused beam across the sample in a straight line generates a 2D cross-sectional image. known as B-scan. The concatenation of the B-scans sections produces a 3D OCT image [21].

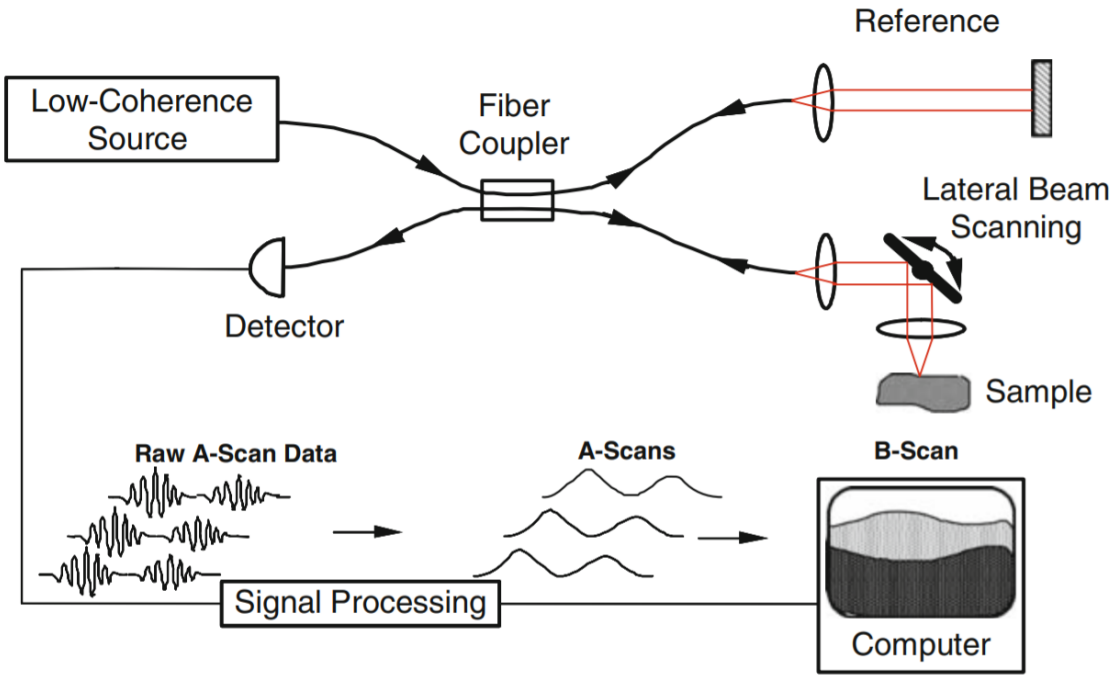

Figure 2.2: Schematic of a generic fiber-optic OCT system. Bold lines represent fiber optic paths, red lines represent free-space optical paths, and thin lines represent electronic signal paths [3]

2.2 Different OCT techniques

In the first generation of OCT systems the image was acquired point-by-point by scanning a laser beam through the sample and repetitively moving the reference arm mirror mechanically [28]. This method known as time-domain OCT (TD-OCT) has a low signal-to-noise ratio (SNR) bounding its A-scan rate to a few kilohertz, due to the coherent noise displayed in all wavelengths caused by the scanning reference delay arm.

The second-generation of OCT introduced spectral interferometry. This technique was named Fourier-Domain OCT (FD-OCT) and is able to get depth information by measuring the interference spectrum in Fourier domain [29]. The reference arm mirror is fixed in a set distance and does

not execute mechanical optical path scanning. The coherent superposition of the back-scattered light from different depths of the sample and the reference generates the interference signal, which is then measured in the form of spectrum, eliminating coherent noise [30]. This detection method was proved to have a powerful system SNR and sensitivity advantage (20-30 dB) over time domain detection [2]. This increased sensitivity corresponds to a faster imaging speed, leading up to a 100 to 1000 times faster acquisition. FD-OCT may be further sub-categorized into two methods: spectral-domain OCT (SD-OCT) and swept-source OCT (SS-OCT).

In SD-OCT, a broad bandwidth low-coherence light source is used, emitting a continuous wave [31]. The recombined interference signal is split according to the optical frequency and measured by a spectrometer. The spectrally-resolved interference fringe pattern is then recorded simultaneously by a linear detector, for instance a line-scan camera. Afterwards, the depth-resolved profile is obtained by executing inverse Fourier transform in the post-processing phase.

In contrast, SS-OCT takes advantage of a rapid wavelength-sweeping light source, that ramps through a range of frequencies [32]. Throughout one sweep, the spectral interference pattern is detected by a high-speed (>100 MHz) photo-detector. This generates a spectral interferogram with fringe patterns, with the frequency content separated in time. The interferogram comprises information regarding every depth layers of the sample simultaneously. Finally, a Fourier transformation is performed to compute the depth profile.

2.3 Challenges in OCT imaging

The nature of multi-dimensional OCT data introduces a whole range of challenges, from the acquisition and manipulation of very large datasets to the processing, analysis and visualization of the data. One of the main problems of OCT, similarly to all coherent imaging techniques, is the inherent image quality corruption due to its optical system design. Fundamentally, speckle noise is the dominating quality degrading factor in OCT images [33]. Its presence can potentially deeply affect the OCT signal and overshadow significant morphological details and features.

2.3.1 Noise in OCT images

The signal-to-noise ratio is a way to measure the image quality, with higher values meaning better quality. The signal-to-noise ratio (SNR) can be defined as: [34]:

$$SNR = \frac{F}{E} = \frac{\sum_{(x,y)} v^2(x,y)}{\sum_{(x,y)} f^2(x,y)} \tag{2.1}$$

where E is the total square value of the noise contribution and F is the total square value of the observed signal.

Commonly, it is represented in the logarithmic scale, in decibels (dB), since differences of signal and noise can have a large dynamic range, being very small or very large:

$$SNR_{dB} = 10log_{10}SNR \tag{2.2}$$

As mentioned previously, speckle noise is the main cause for the degradation of the OCT image quality. As an irregular granular pattern, it is generated by multiple forward and backward scattering of light waves. The speckle is characterized by a Rayleigh distribution [35], that, besides the system's optical properties, can be impacted by the motion of the imaging sample, size and temporal coherence of light source, and aperture of the detector. Speckle is classified as a multiplicative noise, opposed to Gaussian additive noise [36]. A typical retinal OCT image degraded by speckle noise is shown in Figure 2.3

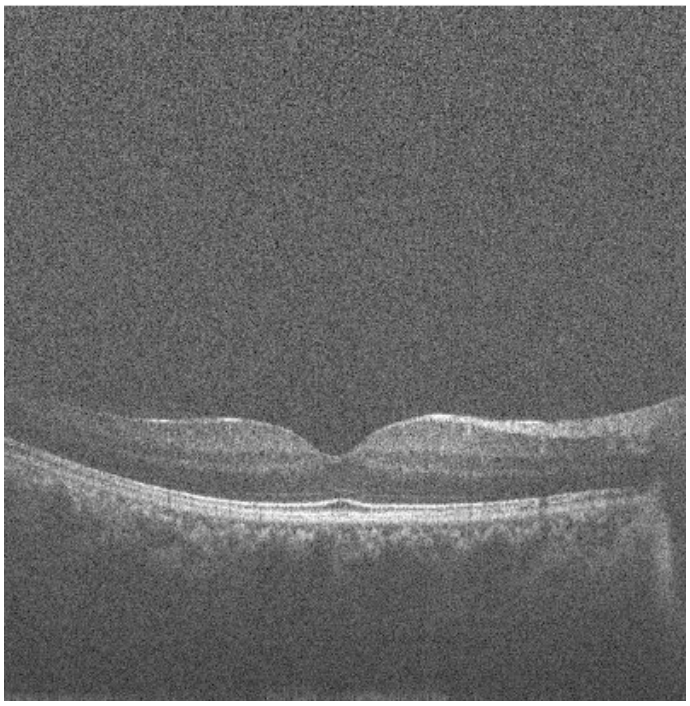

Figure 2.3: Typical retinal OCT image degraded by speckle noise [4]

Numerous OCT denoising techniques, from both hardware and software approaches, have been implemented for reducing speckle noise in OCT images. Without the need to make any changes to the physical system and rising the data acquisition time, post-processing techniques are more favorable. In the next chapter we will dive into some of these techniques. Overall, the choice of a denoising method is application specific, thus an evaluation a priori must be performed in order to select the optimal denoising tool.

Chapter 3

Image pre-processing

Image pre-processing can be viewed as the operations performed on images at the lowest level of abstraction, with intensity images constituting both input and output [37]. These images normally correspond to the original data acquired by the sensor, with an intensity image typically represented by a two-dimensional array or matrix of brightness values, ranging between 0 and 255.

Pre-processing does not increase image information content but usually decreases it [38]. Therefore, from an information handling perspective there is no better pre-processing than no pre-processing - meaning that concentrating on high quality image acquisition is the best way to keep the the most information possible. However, image pre-processing is extremely useful in various situations because information irrelevant in a specific context can be suppressed. Thus, the main goal of pre-processing is the improvement of the image data, by eliminating unwanted distortions or enhancing certain image features meaningful for additional processing or analysis.

The majority of images have significant redundancy of information, enabling image pre-processing techniques to analyze data to discover image properties in a statistical understanding. Such properties can be utilized to suppress undesired degradation like noise or to improve the image. Pixels in the same neighborhood corresponding to actual objects generally possess the comparable brightness value, therefore by picking out a distorted pixel from the image it is possible to recover it as an average value of the neighboring pixels.

Image Pre-Processing techniques can be categorized in four main types [38]:

- Local pre-processing
- Image restoration

In this chapter we will focus on the local pre-processing methods. These techniques achieve a new brightness value of a pixel in the output image by using a small amount of neighbouring points in the input image. Image smoothing methods, Edge detection methods and Morphological operations will be the main methods that we will discuss ahead.

3.1 Image smoothing methods

Image smoothing methods take advantage of redundancy in image data to eliminate noise or other small fluctuations in the image. However, smoothing can also blur sharp image edges so smoothing methods with edge preserving capabilities are preferred. These methods apply averaging in homogeneous local neighborhoods.

One of the most commonly used smoothing methods is the Gaussian filter. It modifies the input image by convolution with a Gaussian function. The 2D Gaussian smoothing operator G(x, y) is given by:

$$G(x,y) = \frac{1}{2\pi\sigma^2} e^{-(x^2+y^2)/2\sigma^2} \tag{3.1}$$

Where σ is the standard deviation of the distribution, that can be adjusted to define the size of the neighborhood on which the Gaussian filter operates. The continuous Gaussian functions have to be subjected to an discretization process in order to be stored as discrete pixels. An integer valued 5 by 5 convolution kernel approximating a Gaussian filter with a σ equal to 1 is displayed in Figure 3.1. An example of an application of the Gaussian filter is shown in Figure 3.2.

$$\frac{1}{273}\begin{bmatrix} 1 & 4 & 7 & 4 & 1 \\ 4 & 16 & 26 & 16 & 4 \\ 7 & 26 & 41 & 26 & 7 \\ 4 & 16 & 26 & 16 & 4 \\ 1 & 4 & 7 & 4 & 1 \end{bmatrix}$$

Figure 3.1: 5-by-5 convolution kernel

Median filtering is another popular smoothing method. This non-linear technique suppresses image noise while avoiding the blurring of sharp edges and can be applied iteratively. The brightness value of the current pixel in the image is replaced by the median of the brightness values in its neighborhood, usually of size 3-by-3 or 4-by-4. The process of Median filtering is demonstrated in Figure 3.3. An example of an application of the Median filter is shown in Figure 3.4.

The median in the neighborhood is unaffected by single noise spikes, thus median smoothing suppresses impulse noise with great success. The major drawback of median filtering in a square neighborhood is the damage on thin lines and sharp corners. However this can be avoided by employing another shape of neighborhood.

(a) Original Image (b) Gaussian Filtered Image

Figure 3.2: Original Image a) Vs. Gaussian Filtered Image with sigma = 2 b)

3.2 Edge detection methods

Edges are locations where the intensity image function experiences abrupt changes. Therefore, edge detectors are local image pre-processing methods able to find changes in the brightness function.

Edge can be considered a property attached to an individual pixel and is a vector variable with two components, magnitude and direction. The edge magnitude is the magnitude of the gradient while the edge direction has an angle of rotation of -π/2 relative to the gradient direction, which provides the direction of maximum growth of the function.

The gradient magnitude

$$|grad\, g(x,y)| = \sqrt{\left(\frac{\partial g}{\partial x}\right)^2 + \left(\frac{\partial g}{\partial y}\right)^2} \tag{3.2}$$

and gradient direction

$$\phi = arg\left(\frac{\partial g}{\partial x}, \frac{\partial g}{\partial y}\right) \tag{3.3}$$

are continuous image functions where arg(x, y) represents the angle (in radians) from the x axis to the point (x, y).

A digital image is discrete by definition so the previous equations, containing derivatives, have to be approximated by difference of the input image g, The first differences in the vertical direction for fixed i and in the horizontal direction for fixed j are determined by:

$$\Delta_i g(i,j) = g(i,j) - g(i-n,j) \quad , \quad \Delta_j g(i,j) = g(i,j) - g(i,j-n) \tag{3.4}$$

Input

1	4	0	1	3	1
2	2	4	2	2	3
1	0	1	0	1	0
1	2	1	0	2	2
2	5	3	1	2	5
1	1	4	2	3	0

Sorted:0,0,1,1,**1**,2,2,4,4

Output

1	4	0	1	3	1
2	1	1	1	1	3
1	1	1	1	2	0
1	1	1	1	1	2
2	2	2	2	2	5
1	1	4	2	3	0

Figure 3.3: Example of Median Filtering with a [3 3] window

where n is a small integer, normally 1, selected to give a good approximation to the derivative while ignoring unimportant alterations in the image function.

Most gradient operators find an approximation for derivatives of the image function using difference. These methods use one or several convolution masks. Some examples are Roberts, Laplace, Sobel, Prewitt, and Kirsch operators.The main drawback of these previous methods is their scale dependence and noise sensitivity.

Canny edge detector is also another popular method optimal for step edges corrupted by white noise. It resembles the Sobel-style gradient magnitude and direction techniques, but goes further and some additional post-processing to clean up the edges is performed.

Another category of operators are established on zero-crossings of the image function second derivative. These methods are more robust than small-size gradient detectors and can be calculated as a Laplacian of Gaussians (LoG) or as a difference of Gaussians (DoG) [39].

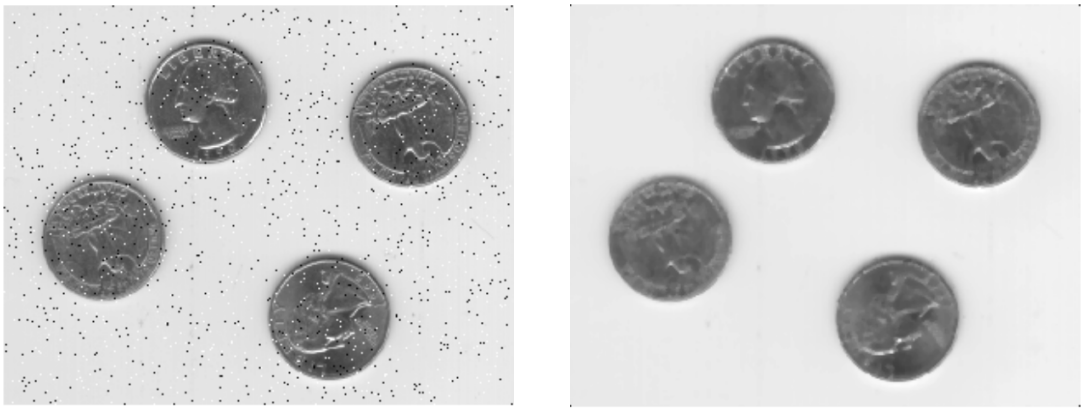

(a) Original Image (b) Median Filtered Image

Figure 3.4: Original Image a) Vs. Median Filtered Image with neighborhood size = [3 3] b)

3.3 Morphological operations

Mathematical morphology is a broad set of image processing operations that aims to alter the shape or morphology of features in an image. Through non-linear operations, the image is changed, presumably for the better, by suppressing shape noise or outliers and strengthening predominant shape characteristics [40].

Morphological operations are usually applied to binary images, whose pixels can have one of exactly two colors, normally black and white. These images may contain numerous imperfections, such as noise and distortions caused by simple thresholding. Therefore, morphological operations are used to eliminate these imperfections, taking in consideration the form and structure of the image [41]. For example, isolated pixels could be removed and thin features could be enlarged while preserving the main shape.

Morphological operations establish a relation between an image and a small shape or template named structuring element. It guides the morphology process by specifying the surrounding pixels utilized in the processing of each pixel. Moving the structuring element systematically across the entire image, an output image is obtained by storing the result (either zero or one) of the its relation with the image in each position.

The structuring element is a small matrix, whose elements can be either 0 or 1 :

- The matrix dimensions define the size of the structuring element.
- The distribution of zeros and ones defines the shape of the structuring element.
- The structuring element is expressed with respect to a local origin, that may be located outside of the structuring element.

Two types of structuring elements at different sizes are shown in Figure 3.5. Some operations evaluate if the structuring element "fits" within the neighbourhood, while others test if it "hits" the neighbourhood. These methods revolve around checking for each ’1’ in structuring element if the pixel at the same position in the input image is also a ‘1’. If this is true for at least one of its pixels, the structuring element hits the image at the current pixel position. On the other hand, if this is true for all of its pixels, the structuring element fits the image at the current pixel position.

The fundamental operators of morphology include dilation, which expands objects, and erosion which shrinks them [42]. From a combination of these two, more complex morphological operators are obtained, for instance opening and closing. In any case, the number of pixels altered from the objects in an image is dependent on the size and shape of the structuring element applied.

3.3.1 Fundamental operations

Dilation is a morphological operation that adds pixels to the boundaries of objects in an image, turning them more visible and filling in small holes [5]. The dilation of an image f by a structuring

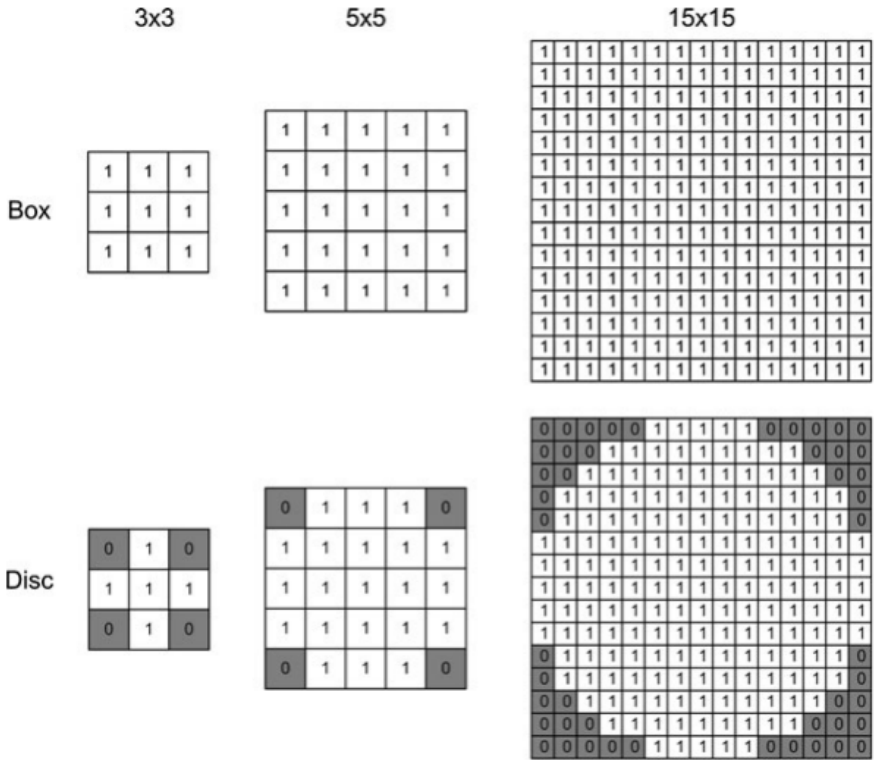

Figure 3.5: Two types of structuring elements at different sizes [5]

element s that generates a new binary image g is given by

$$g = f \oplus s \tag{3.5}$$

In the output image g, the value of the output pixel is the maximum value of all neighbouring pixels. This means that when moving the structuring element s across the entire image, if it hits the input image f, the value of the output pixel in the current location of the structuring element's origin (x,y) will be equal to one, i.e. g(x,y) = 1 if s hits f and 0 otherwise, reiterating for all possible coordinates (x,y). An example of dilation of a binary image using a structuring element 3-by-3 is shown in Figure 3.6.

Erosion is a morphological operation that removes pixels on object boundaries, eliminating islands and small objects so that only significant objects are preserved [5]. The erosion of an image f by a structuring element s that generates a new binary image g is given by

$$g = f \ominus s \tag{3.6}$$

In the output image g, the value of the output pixel is the minimum value of all neighbouring pixels. This means that when moving the structuring element s across the entire image, if it fits the input image f, the value of the output pixel in the current location of the structuring element's origin (x,y) will be equal to one, i.e. g(x,y) = 1 if s fits f and 0 otherwise, reiterating for all possible

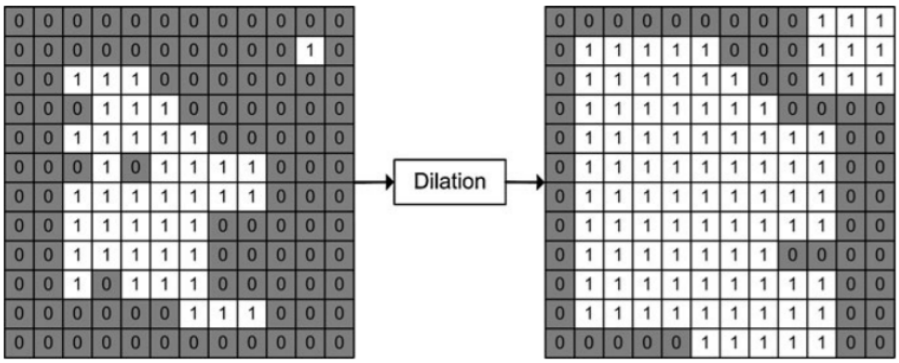

Figure 3.6: Dilation of a binary image [5]

coordinates (x,y). An example of erosion of a binary image using a structuring element 3-by-3 is shown in Figure 3.8.

3.3.2 Compound operations

The different combinations of dilation and erosion leads to many complex morphological operations useful to image processing. These are designated compound operations. The two most popular compound operations are opening and closing.

Opening is a morphological operation that deals with the decreased object size when using erosion to erase small noisy objects or fractured parts of bigger objects [5]. Indeed, it only removes small objects or narrow lines from the image while preserving the size and shape of objects of bigger dimensions in the image. The opening operation performs an erosion on image f followed by an dilation on the eroded image, using the same structuring element s for both operations. The output image g is given by:

$$g = f \circ s = (f \ominus s) \oplus s \tag{3.7}$$

Closing is a morphological operation that deals with the increased object size when using dilation to fill the holes in objects [5]. Indeed, it fills small holes from an image while preserving the size and shape of objects in the image. The closing operation performs a dilation on image f followed by an erosion on the dilated image, using the same structuring element s for both operations. The output image g is given by:

$$g = f \bullet s = (f \oplus s) \ominus s \tag{3.8}$$

Both opening and closing are idempotent operations. This means that they can only be applied once with the same structuring element. The same operation applied again have no further effect on that image [40].

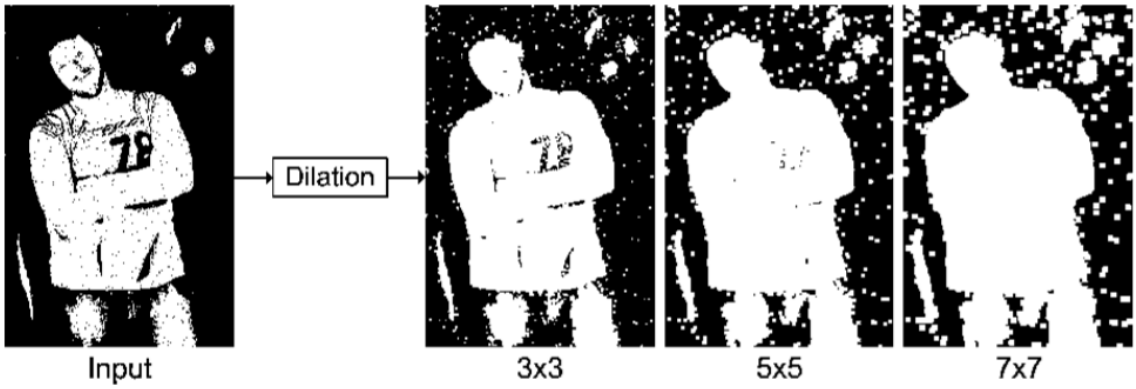

Figure 3.7: Dilation of a binary image with different structuring elements [5]

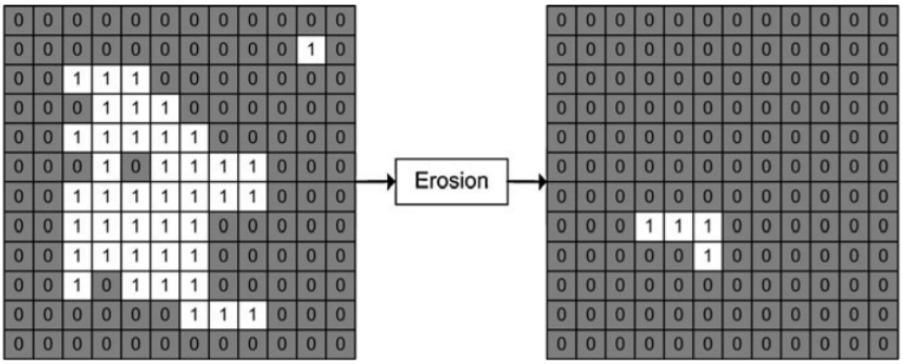

Figure 3.8: Erosion of a binary image [5]

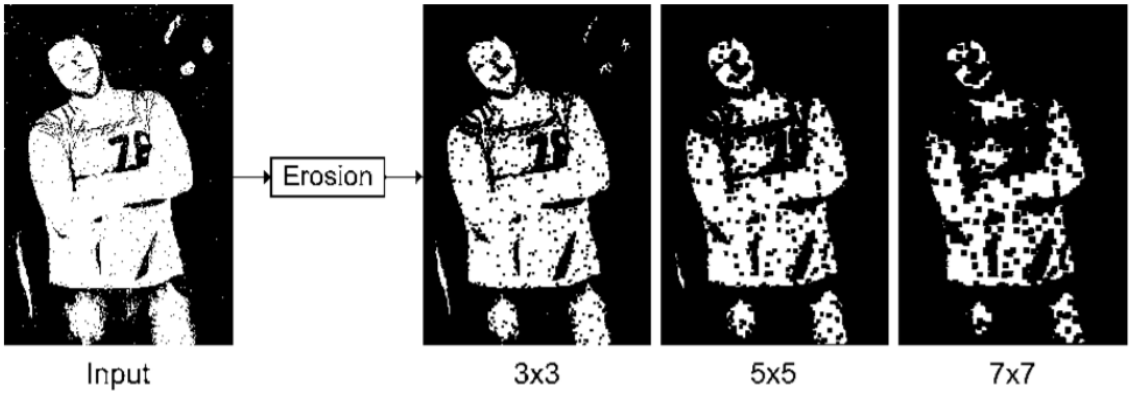

Figure 3.9: Erosion of a binary image with different structuring elements [5]

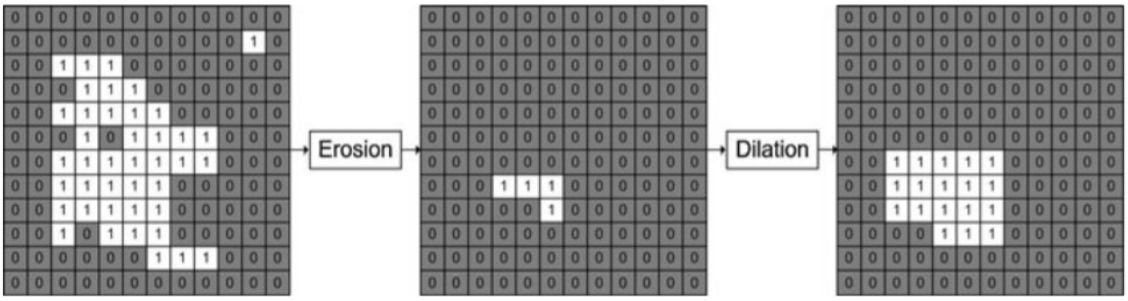

Figure 3.10: Opening of a binary image [5]

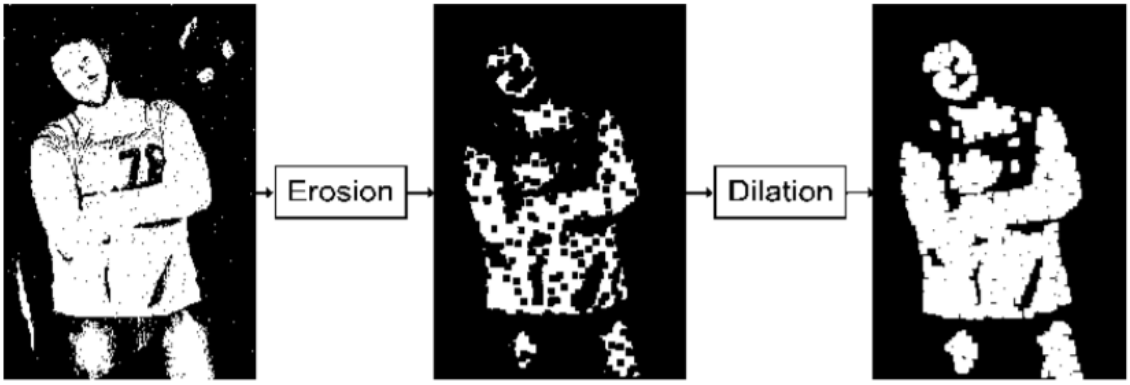

Figure 3.11: Example of the opening method applied on a binary image [5]

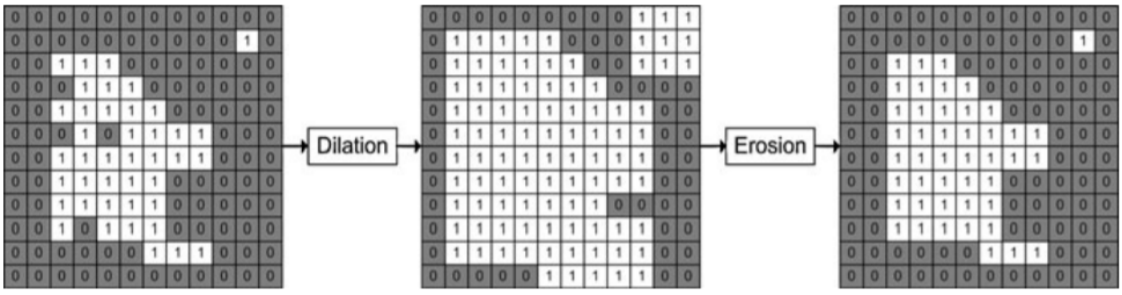

Figure 3.12: Closing of a binary image [5]

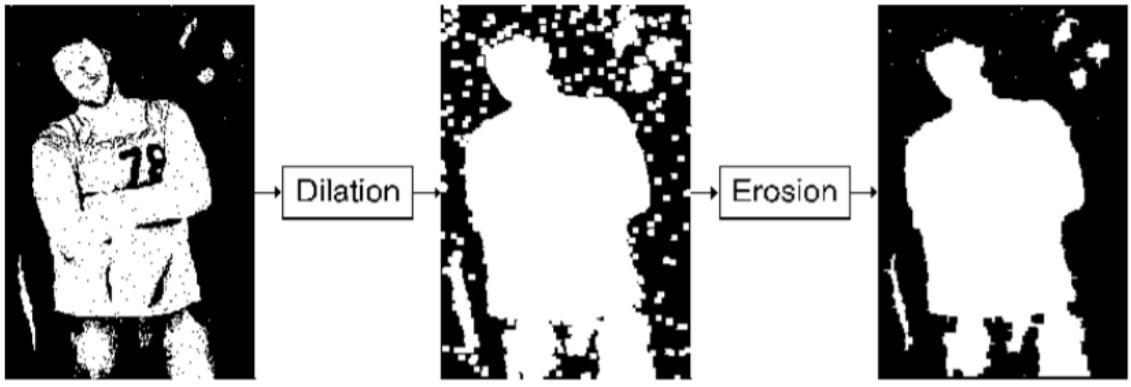

Figure 3.13: Example of the closing method applied on a binary image [5]

Chapter 4

Image stitching

Image stitching is the process of combining and blending multiple images with overlapping areas to form a new panoramic image of high resolution [43, 44]. However, the majority of image stitching methods require exact overlap between images and identical exposure to deliver optimal results. This process can be divided in three steps- image calibration, image registration and image blending.

Image Calibration reduces the variations that may happen between an ideal lens model and actual camera lens model used [43]. By calibrating the pixels to be stitched, it provides a correction for deformations and exposure differences.

Image registration can be defined as a process that transforms different sets of images into a particular coordinate system [43]. These images may have been captured by different imaging equipment or lens or even taken at distinct time intervals and viewpoints. Through this process, points in two separate images that match the same anatomical point are mapped to one another.

Image blending involves the execution of the adjustments identified in the calibration stage as well as the seamless stitching of the images in the overlapping area [43]. This process blends the images together, correcting the seam line to minimize the intensity difference of overlapping pixels.

4.1 Image registration

The goal of image registration is to overlay two or more images of the same object that may differ due to differences in acquisition times, angles, scene and/or sensors used. It geometrically aligns two images: the stationary one is named reference image, while the ones being shift relative to the reference image are named target images [45].

Image registration techniques follow two main approaches: feature-based methods and area-based methods [46]. Feature-based techniques selectively extract sparse feature points and then perform a comparison between them. On the other hand, area-based techniques estimate a correspondence between images using a fixed size window or even entire images.

Feature-based methods first identify main feature points of each image. Subsequently, a comparison between the two sets of features is made and common features between a reference image and a target image are determined. Finally, a point-by-point mapping between them is estimated. This process is based on correlating points, lines, edges, corners or other shapes [46]. These features should be consistent over time, distinct, well distributed across the image and efficiently detectable in both images. The most prominent feature-based techniques are Harris [47], Scale-Invariant Feature Transform (SIFT) [48], Speeded Up Robust Features (SURF) [49] and ORB [50]. These methods have a high degree of robustness and are invariant to image scale, translation and rotation. However, it is hard to find prominent features in OCT images so an automatic 3D feature selection algorithm is difficult to implement.

Alternatively, area-based methods are established on a statistical comparison between a small window of points in the reference image and windows of equal size in the target image. After finding the window in the target image which best matches all potential windows in the reference image, their respective centers are taken as the control points. Later, control points are utilized to calculate the transformation parameters [45]. This comparison employs similarity metrics, that evaluate the similarity between the windows, and is maximized across the entire potential candidate matches selection. The comparison can be performed either in the spatial domain with Normalized Cross-Correlation (NCC) or in the frequency domain with Phase Correlation [51]. These methods are able to successfully register images by utilising all image information, but their application is greatly limited to images taken in the same plane, allowing only shift and small rotation between the images.

4.1.1 Normalized Cross-Correlation

Normalized cross-correlation is an image registration method commonly used for template matching or pattern recognition. It detects a sub-image in the reference image that constitutes the best match for the selected template [52]. Let I be the reference image with the size of M*N pixels, and t be the template image with the size of m*n pixels, where t is small compared to I. As illustrated in Figure 4.1, the template image t slides on the reference image I, and the similarity between template t and sub-image f(x,y) is measured by using the normalized cross-correlation function when the template t slides to the position (u,v). The normalized cross-correlation between them is given by:

$$C(u,v) = \frac{\sum_{x,y}\left[f(x,y) - \overline{f_{u,v}}\right]\left[t(x-u,y-v) - \bar{t}\right]}{\left\{\sum_{x,y}\left[f(x,y) - \overline{f_{u,v}}\right]^2 \sum_{x,y}\left[t(x-u,y-v) - \bar{t}\right]^2\right\}^{0.5}} \tag{4.1}$$

where f(x,y) is the pixel value of the reference image I at (x,y), t(x,y) is the pixel value of the template image t at (x,y), $\bar{t}$ is the average pixel value of the template image t and $\overline{f_{u,v}}$ is average pixel value of f(x,y) in the region under the template. It should be pointed that in Equation 4.1, both images are subtracted by the respective mean followed by a division by their standard deviation prior to calculating cross-correlation. This normalization step can increase performance and accuracy in template matching when f and t possess different local intensities levels.

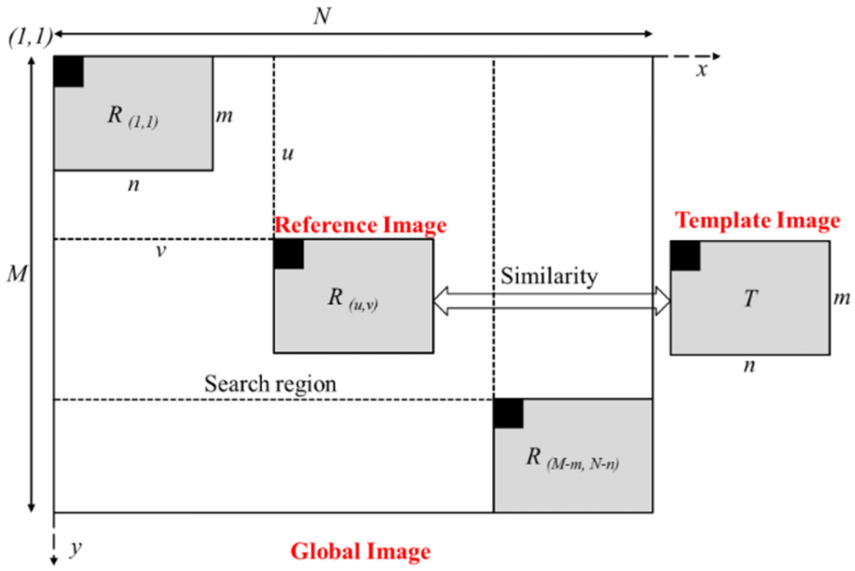

Figure 4.1: Principle of template-matching [6]

Finally, a correlation map C is generated by computing NCC for all possible sub-images f in the reference image I by moving the template image t across the whole reference image. The peak on the cross-correlation map indicates the best match position, denoting the position of t in I.

4.2 Image blending

Image blending techniques aims at blending multiples images into a single seamless image, taking into consideration their overlapping areas [53, 54]. Merging two different image without an appropriated blending algorithm, usually by attaching the source image onto a target image, may generate an unnatural output image. The seam can be very noticeable, making it particularly bothering. Therefore, image blending focuses on producing a final blended image with a more natural look of the the merged area, with both input images having a fitting contribution to the output image. One example that can be used to show the effectiveness of image blending methods is presented below. In Figure 4.2 we have the original images that we pretend to blend, one of an apple and one of an orange. If we simply put the images together, we get an image with sharp edges and a visible seam, shown in Figure 4.3 a). A final image obtained after using image blending methods is shown in Figure 4.3 b), where the sharp edges and the seam are visibly less notable.

The image blending process normally only takes place in the overlapping regions, which are established on the stitching phase [55]. When the overlapping areas between input images are substantial, and their intensity values in these areas do not fully match, some degree ghosting or 'blurring' can be perceptible in the output image. On the other hand, when the overlap is limited to a small area, the seams can be obvious in the output image. Therefore, to smooth the transition between two images and create a single seamless panoramic image, multiple image blending methods have been proposed.

(a) Original Image Apple

(b) Original Image Orange

Figure 4.2: Original Image Apple a) and Original Image Orange b)

(a) Final Image not blended

(b) Final Image blended

Figure 4.3: Final Image not blended b) vs Final Image blended b)

The most simplistic image blending method is just averaging the intensity value of the pixels from both images in the overlapping region [56]. Considering a pair of images $I_1(x,y)$ and $I_2(x,y)$ with an overlapping area $A_{I_1,I_2}(x,y)$, in the blended image $I_{blended}$, the intensity value of a pixel situated at (i, j) $\subseteq A_{I_1,I_2}$ would be the average intensity of the corresponding pixels from I_1 and I_2:

$$I_{blended}(i,j) = \frac{1}{2}(I_1(i,j) + I_2(i,j)) \tag{4.2}$$

In this work, we propose an image blending process on the basis of the distance of the pixel in the overlapping area to the nearest non-overlapping pixel in both images. Considering again a pair of images $I_1(x,y)$ and $I_2(x,y)$ with an overlapping area $A_{I_1,I_2}(x,y)$, the blended image is computed through a weighting system establish on the distances of the pixel in hand to the closest non-overlapping pixel from both images. The main idea of this blending method is to give more weight to the intensity of the pixel closer to the non-overlapping area. So, if a pixel in the overlapping region is far from the non-overlapping region in the first image but is closer from the non-overlapping region in the second image, its intensity in the blended image will be closer to the intensity of the pixel in the second image. In the blended image $I_{blended}$, the intensity value of a pixel situated at (i, j) $\subseteq A_{I_1,I_2}$(i, j) depends on both the distance to the non-overlapping pixel in image $I_1(x,y)$, $d_1(i,j)$, and the distance to the non-overlapping pixel in image $I_2(x,y)$, $d_2(i,j)$:

$$\begin{aligned} I_{blended}(i,j) &= I_1(i,j)w_1(i,j) + I_2(i,j)w_2(i,j) \\ w_1(i,j) &= 1 - \frac{d_1}{d_1 + d_2} \\ w_2(i,j) &= 1 - \frac{d_2}{d_1 + d_2} \end{aligned} \tag{4.3}$$

where the condition below is satisfied:

$$w_1(i,j) + w_2(i,j) = 1 \tag{4.4}$$

Note that for both $w_1(i,j)$ and $w_2(i,j)$ the fraction is subtracted from one since the value of a pixel in the overlap area close to the non-overlapping area in a certain image should be more similar to the value of the corresponding pixel in the image in question.

Chapter 5

System components and configuration

The OCT imaging within an industrial context is quite distinct from the imaging done in a controlled environment like a laboratory since it is not isolated from vibration and temperature. The structures to image have a different geometry and much bigger dimensions compared to common surfaces where OCT systems are applied; in most cases, the imaging is performed in very specific and small areas, for example the retina or coronary arteries in the medical field. When imaging an object with a circular symmetry a conventional OCT setup is not sufficient.

Since the Field of View of an OCT system is small, to build a complete 3D OCT image of an object of sizeable dimensions, like a glass cup or a water bottle, we need to incorporate some type of movement, either from the object or the imaging system. In the beginning of the project, due to its simplicity a rotational stage would be utilized. This would allow a greater focus on the data processing part and a proper calibration of the OCT system. Later, the goal would be the implementation of the system with a robotic arm, making it applicable in an industrial environment. Here instead of moving the object itself, we move the imaging system, by attaching the sample arm of the interferometer on the robotic arm. Obviously, this will make the problem much more complex, depending on the robot's degrees of freedom.

This later part of the project would be possible because the OCT system that we intended to use, an infrared-light OCT system, had a movable sample arm. So, the planned final system setup was the infrared-light OCT system combined with a robotic arm. However, during our work we faced a problem with the trigger of the camera of the infrared-light OCT system. In fact, the trigger speed of the camera was extremely inconsistent and did not match the value defined by the control software, up to the ten times slower than the demanded. Therefore, the infrared camera could not be triggered and controlled correctly rendering the use of the infrared-light OCT system impossible. So we had to switch and continue our work with another system, a visible-light OCT system. This new system is very sensitive due to its design and its setup doesn't allow any movement of the sample arm so the implementation with the robotic arm was not possible. Therefore, our final system setup was the visible-light OCT system combined with a rotational stage.

In this chapter we give an overview of the system components used during our work. We also

describe their respective control software and their integration within the system. Regarding the system components, note that we will present the two OCT systems, one with an infrared light source and one with a visible light source. We will also detail the characteristics of a rotational stage and a robotic arm. Finally, we will describe how to control the OCT systems, the rotational stage and the robotic arm and how to integrate these components.

5.1 System components

5.1.1 Infrared-light OCT system

The infrared-light OCT system consist in a fiber-based interferometer, some free space components, an SLD as a light source and a spectrometer. The SLD light source is a broadband SLD centered around 1550 nm with a bandwidth of 50 nm and a total output power of 22 mW (Thorlabs – S5FC1005S). The light from the SLD is injected into the interferometer using a broadband circulator (Thorlabs - 6015-3-APC). The circulator acts as a protection for the SLD as it avoids any light returning into the light source. The interferometer is a Michelson interferometer based on a broadband fiber coupler (Thorlabs - TW1550R5A2). The reference path of the interferometer is made of flat mirror (Thorlabs - PF10-03-G01) mounted a on translation stage (Thorlabs – SM1ZA). The sample arm of the interferometer consists of a pair of galvo-scanner (Thorlabs – GVS012/M), a pair of achromatic lenses (Thorlabs – AC254-030-C-ML) acting as a telecentric configuration and an objective lens (Thorlabs -– AC254-030-C-ML). The spectrometer is sensitive from 1500 nm up to 1600 nm and has a maximum linerate of 1 kHz (Ocean Optics – NIR Quest 512). A photo of the infrared-light OCT system can be seen in the Figure 5.1

5.1.2 Visible-light OCT system

The visible-light optical coherence tomography system used in this dissertation is established on four major components, shown in the Figure 5.2 [7]. First, the system adopts a supercontinuum light source (Electro VISIR- Leukos (France)), with a full spectrum that spans from 450 nm to 2400 nm and a total optical power near 200 mW. Using bulk optical filters, it is filtered to illuminate the interferometer with visible light, for wavelengths from 450 nm up to 700nm and roughly 8 mW of optical power. Second, the interferometer is a Michelson interferometer, based on bulk optics. Third, the spectrometer used is a ultra-broad spectrometer (COBRA VIS – Wasatch Photonics (United States)), with a sensitivity bandwidth spanning from 500 nm to 700 nm. Finally, there is a custom designed interface implemented on LabView 2020, which provides a communication route between multiple active components (Galvo-scanner, Digital-to-Analog converter, etc.) for data acquisition. A photo of the visible-light OCT system can be seen in the Figure 5.3

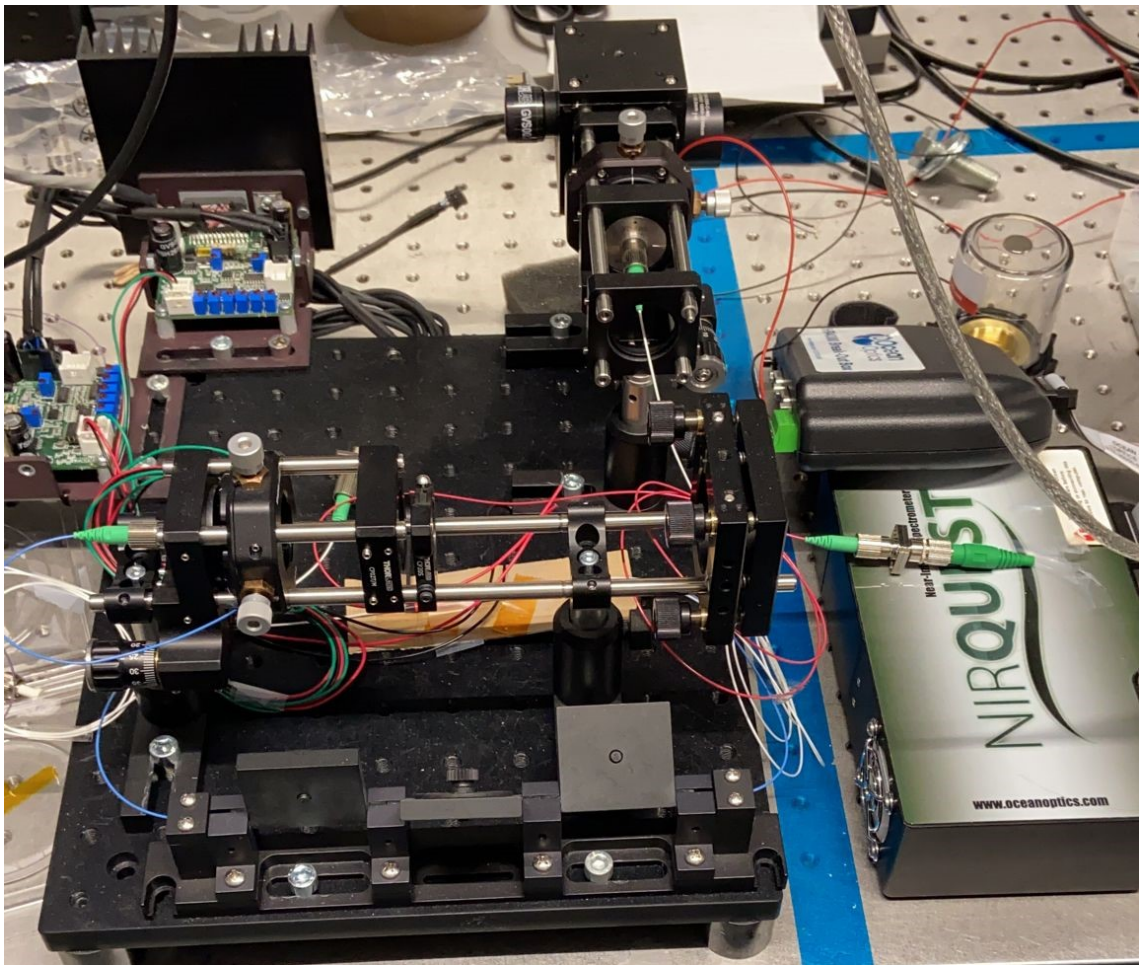

Figure 5.1: Infrared-light OCT system

5.2 Rotational stage

The rotational stage model used during this work was CR1-Z7, by Thorlabs [57], shown in the Figure 5.4. This motorized rotation stage offers high-precision continuous 360º motion. Utilizing a 256:1 gear reduction head, the rotator provides minute movements over the entire travel range. The reduced backlash worm gear design combined with a high-resolution optical encoder (12,288 pulses/rev) allows a high rotational precision, achieving a minimum rotational angle of 0.0006º or 2.16 arcsec. The high torque 12 VDC servo motor provides sufficient power to rotate vertical loads up to 25 lbs. The speed range is between 22 arcsec/sec and 6º/sec. By rotating the rotational stage using a small angle, we are shifting the surface being target by the OCT system. Therefore, after a full 360º rotation and scanning the surface on each small rotation, we have imaged the complete surface of the object and the small field of view problem of an OCT system was solved.

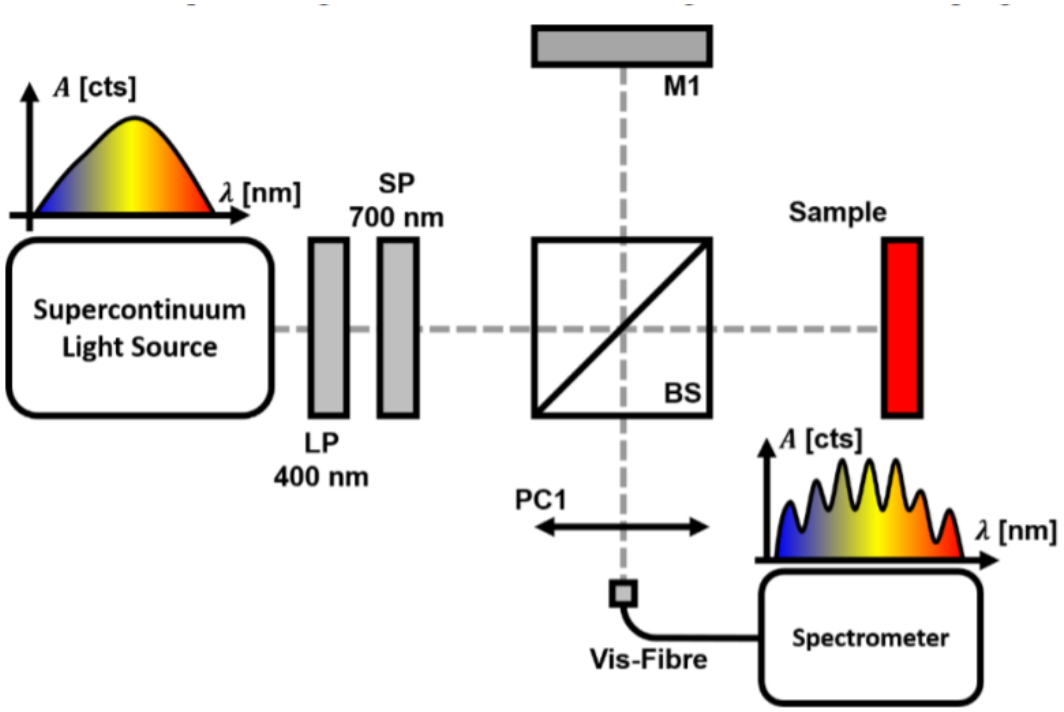

Figure 5.2: Schematic representation of the visible OCT system. LP: Long Pass filter, SP: Short Pass filter, BS: Beam Splitter, M1: Flat Mirror, PC1: Parabolic Collimator, Vis-Fiber: Optical Fiber for visible light and A is the signal amplitude [7]

5.3 Robotic arm

The robot model used is the ABB IRB-1200 [58], which is a 6-axis robot arm and offers a 5.0 kg payload and 901 mm reach. Offering a compact design, the main application for the robot are Material Handling and Small Parts Assembly. The ABB IRB-1200 has a good position repeatability, achieving 0.02 mm. It is shown in Figure 5.5

5.4 System control

5.4.1 OCT system control

Both OCT systems are controlled using LabVIEW. A diagram of the program can be seen in Figure 5.13. The program can be divided in two main loops that are running continuously: the control loop and the saving loop. The control loop is responsible to setup all parameters and initialize the necessary tasks to acquire the data. In the acquire data phase, the spectrum values are read and later this acquired data is saved as an element in a queue that will be passed to the saving loop, where each element of the queue are dequeued and saved to a file.

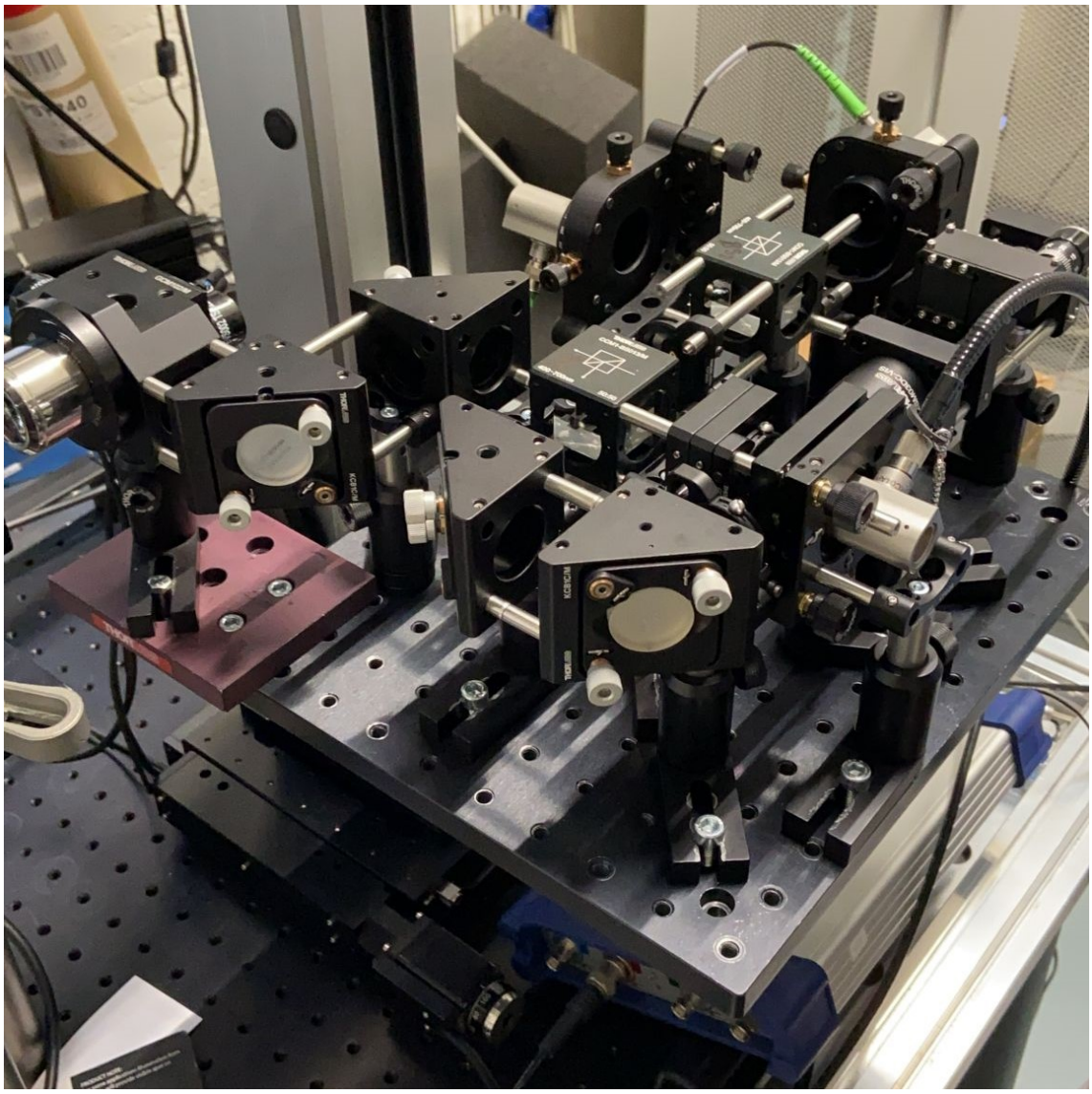

Figure 5.3: Visible-light OCT system

Figure 5.4: CR1-Z7 motorized rotation stage

Figure 5.5: Robotic arm ABB IRB-1200

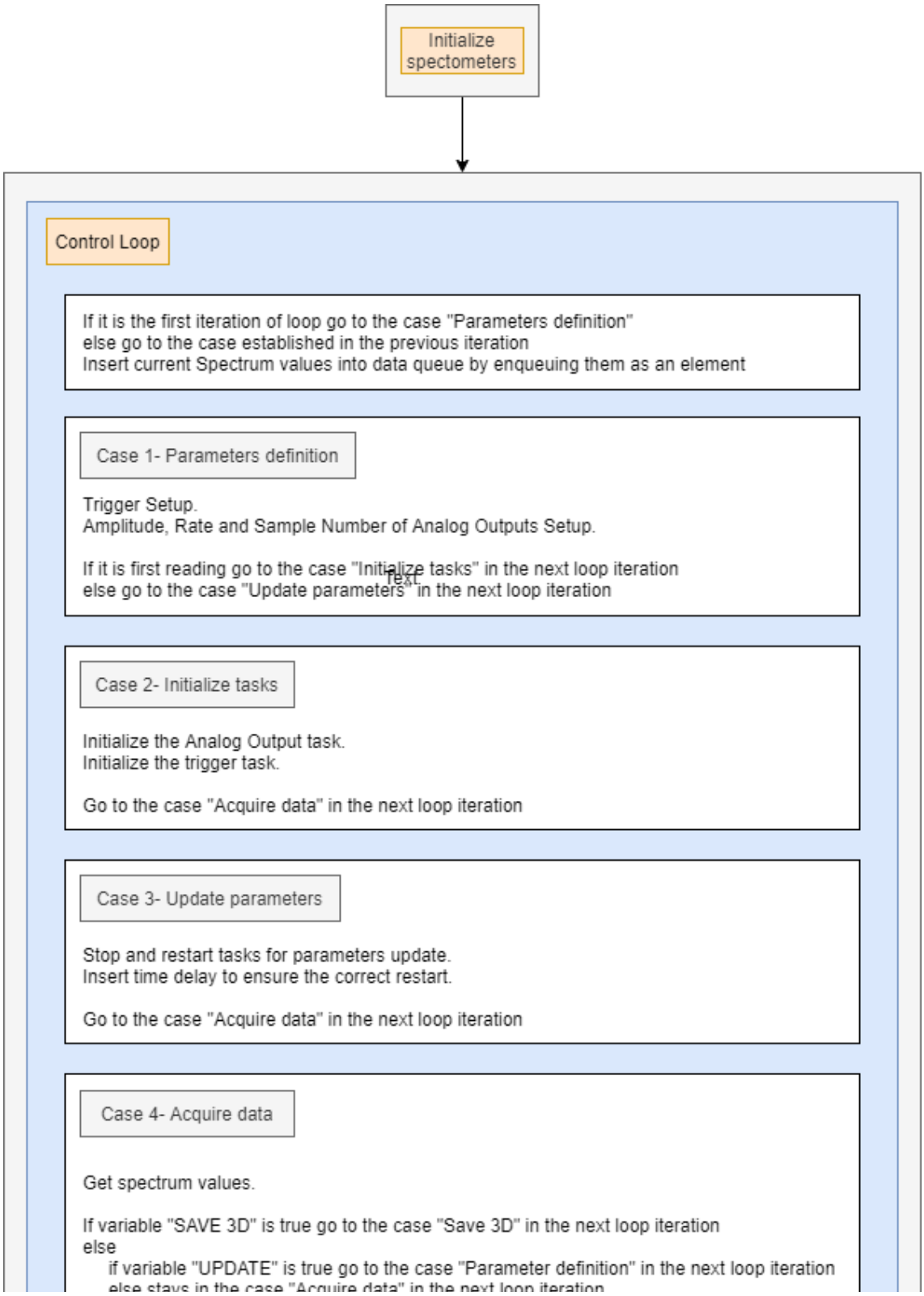

Figure 5.6: Control of OCT system. Continues in next page.

Go to the case "Acquire data" in the next loop iteration

Case 4- Acquire data

Get spectrum values.

If variable "SAVE 3D" is true go to the case "Save 3D" in the next loop iteration
else
if variable "UPDATE" is true go to the case "Parameter definition" in the next loop iteration
else stays in the case "Acquire data" in the next loop iteration

Case 5- Save 3D

The tasks are stop and restarted at a correct position.
Insert time delay to ensure the correct restart.
Set value of variable "SAVE" to true.

Go to the case "Acquire data" in the next loop iteration

Case 6- Stop

Stop taks before stopping execution to protect motor and camera
from abrupt voltage cut

Stays in the case "Stop" in the next loop iteration

If variable "STOP" is true go to the case "Stop" in the next loop iteration

Saving Loop

If variable "SAVE" is true
Counter = Counter + 1
Set "FILE NAME" and "PATH TO SAVE".
Create the new file.
Dequeue element from the data queue and write the data to a file.
Close the file reference.
If Counter >= Number_Of_Images, set variable "SAVE" to false

5.4.2 Rotational stage control

The rotational stage was controlled using LabVIEW. Different methods were implemented to rotate the stage. First, an absolute rotation was implemented so we could reach a certain degree position. After, a relative rotation was implemented so we could rotate a certain amount. Finally, a periodic rotation was implemented so we could rotate a certain amount every x seconds.

The complete front panel with all the controls and displays and can be seen in Figure 5.7.

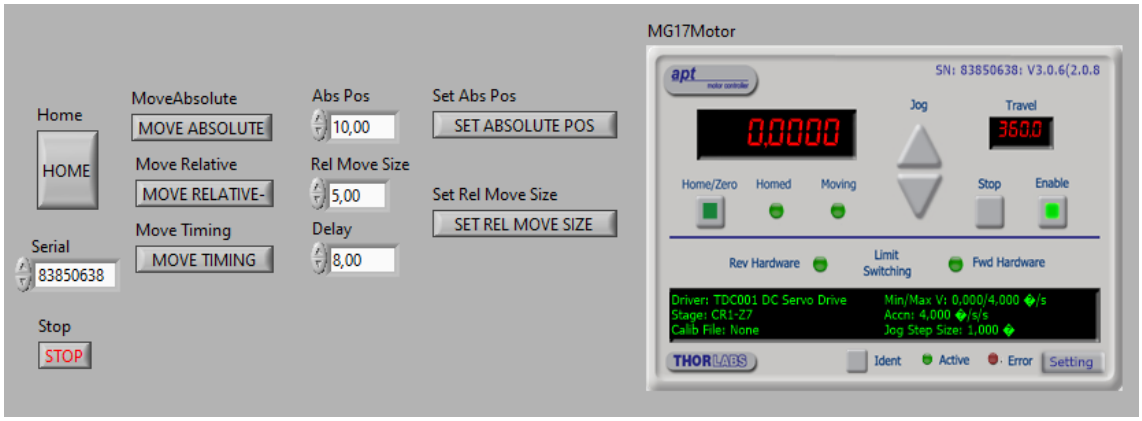

Figure 5.7: Front panel

Before programming the moving of the rotational stage, the "MoveHome" function was implemented. It resets the position of the stage, so its current position becomes the position 0. The block diagram is shown in Figure 5.8.

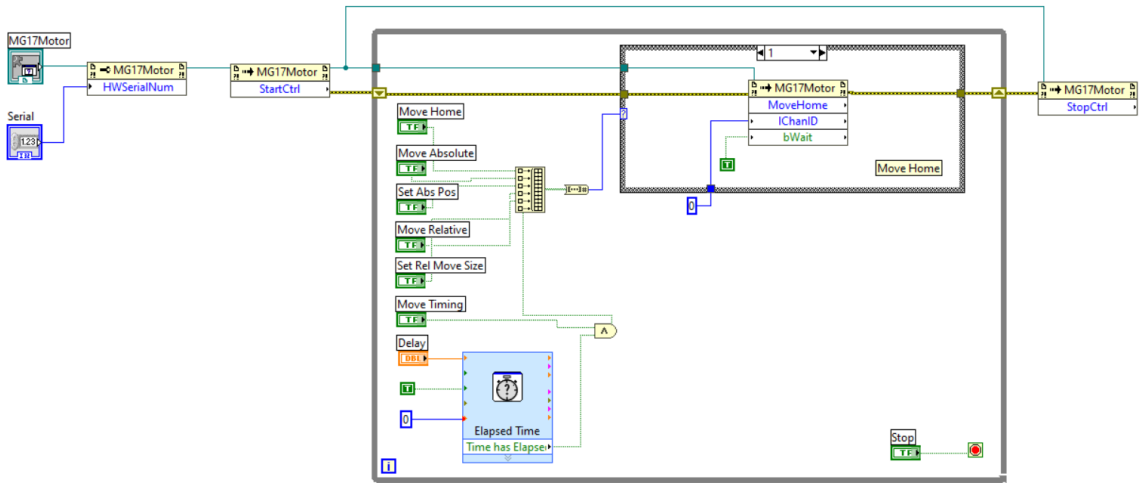

Figure 5.8: "MoveHome" block diagram

After, an absolute rotation was achieved with the "Set Abs Move Pos" and "Move Absolute" functions. The former sets the desired absolute position while the later executes the movement to said position. The block diagram is shown in Figure 5.9.

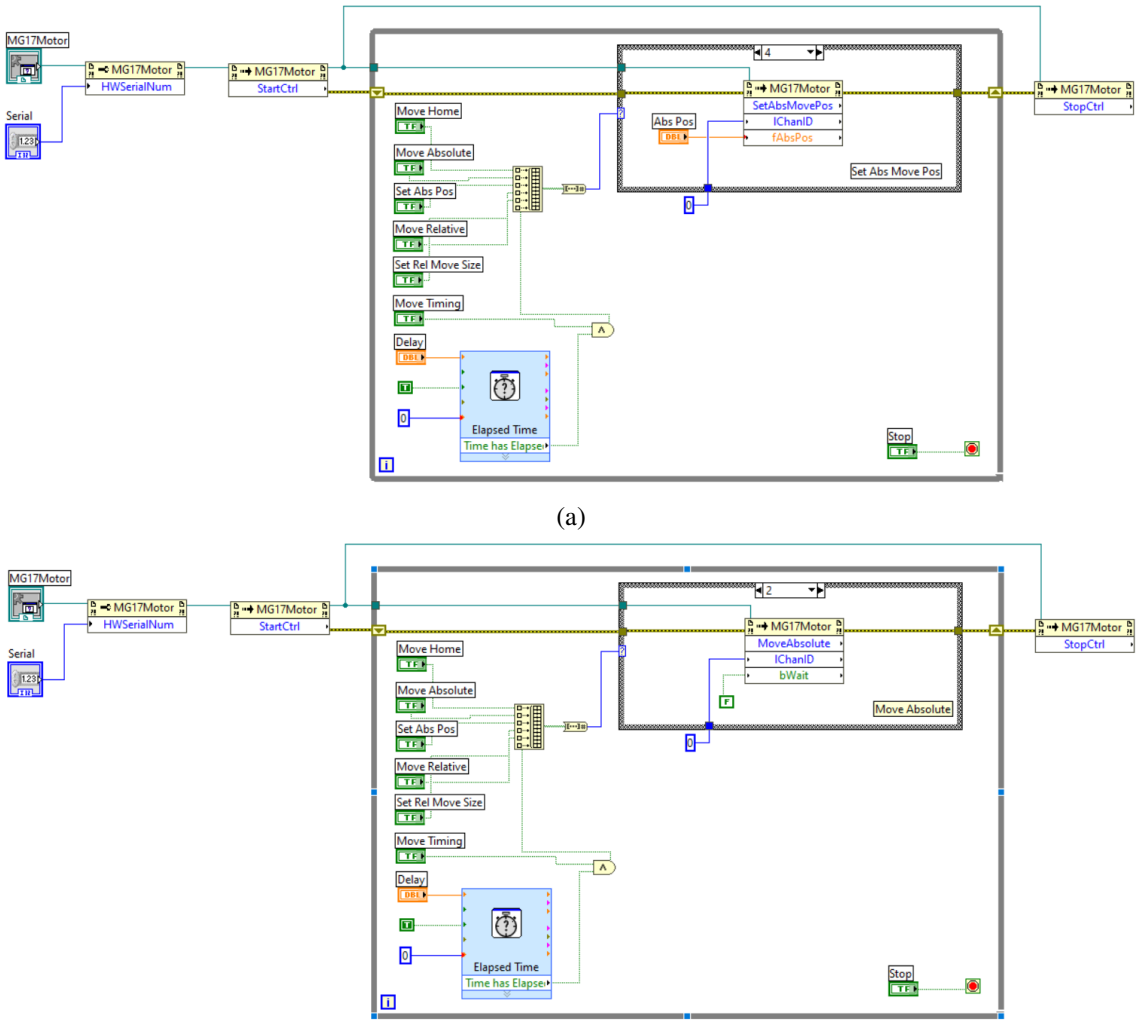

Figure 5.9: "Set Abs Move Pos" block diagram (a) and "Move Absolute" block diagram (b)

Later, a relative rotation was obtained with the "Set Rel Move Size" and "Move Relative" functions. The first sets the desired relative moving amount while the later executes the movement itself. The block diagram is shown in Figure 5.10.

Finally, a periodic rotation was obtained with the "Move Timing" function. While still requiring the "Set Rel Move Size" to define the relative moving amount, now is necessary to set a time delay, which will be given as an input to Elapsed time VI. The block diagram is shown in Figure 5.11.

5.4.3 Robotic arm control

The robotic arm is controlled using ROS. ROS is an abbreviation for Robot Operating Systems. It is an open-source framework designed for the conception of software for robots, being the most popular framework for programming robots []. In our project, it will be used to program and

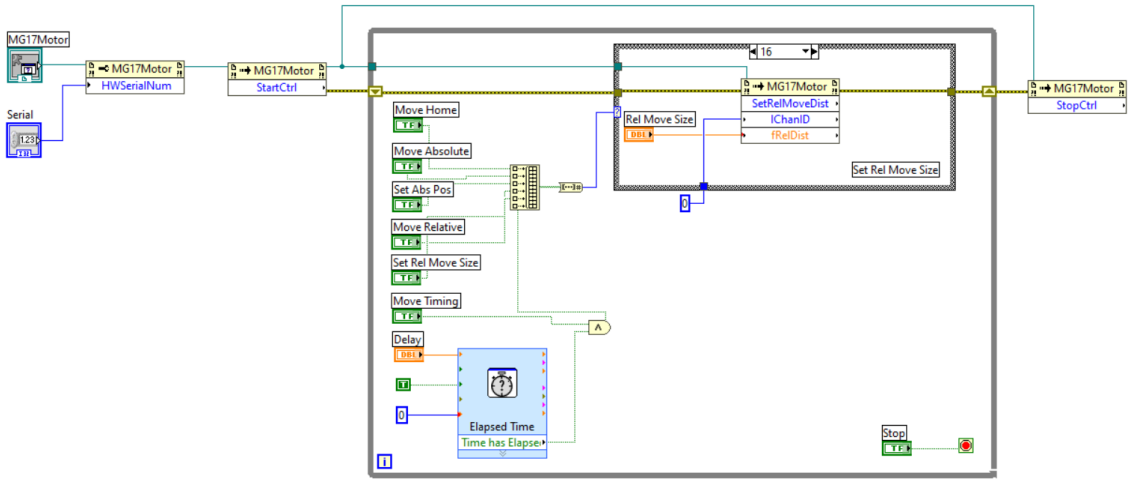

(a)

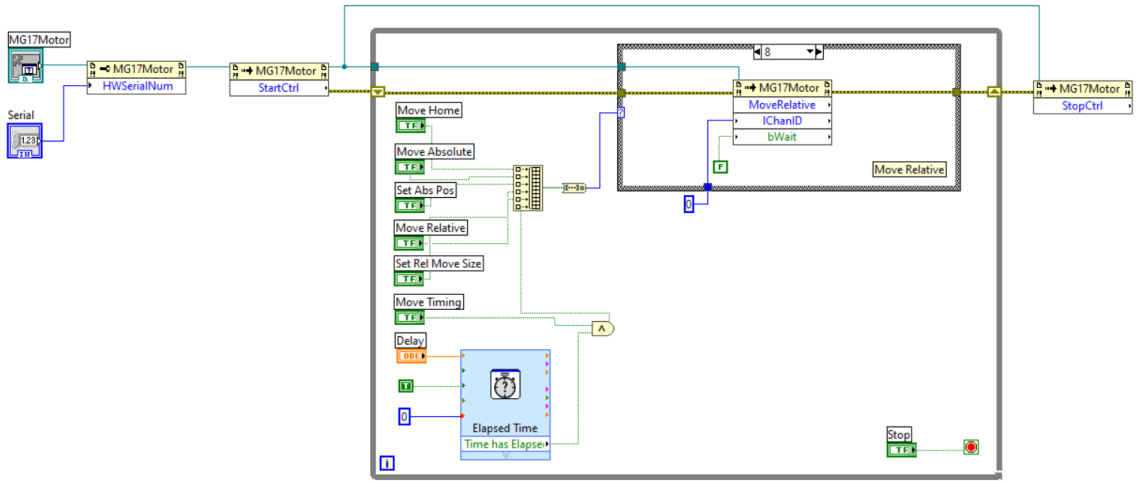

(b)

Figure 5.10: "Set Rel Move Size" block diagram (a) and "Move Relative" block diagram (b)

control the robotic arm. The version that will be used is ROS Noetic Ninjemys, the 13th and latest distribution release of ROS, that was made available on May 23, 2020 by Open Robotics, the developer of ROS [59].

Main features ROS are the nodes, the topics, the services and the messages [60], and their relationships are illustrated in Figure 5.12.

A node is a process that makes computations according to its role, the task it corresponds to. The different nodes are combined in a graph where they communicate with each other via the topics and services. In general, one application will involve multiple nodes. The task represented by a node can be for example the perception of the environment using a camera or laser scanner, the route planning, the battery level monitoring, or the control of the wheels' motors speed.

A node, to communicate with each other, can subscribe or publish to a topic. A node that publishes to a topic sends data to this topic. Every node subscribed to this topic will have access to this data. There can be multiple subscribers and publishers to one topic, and the data is anonymized,

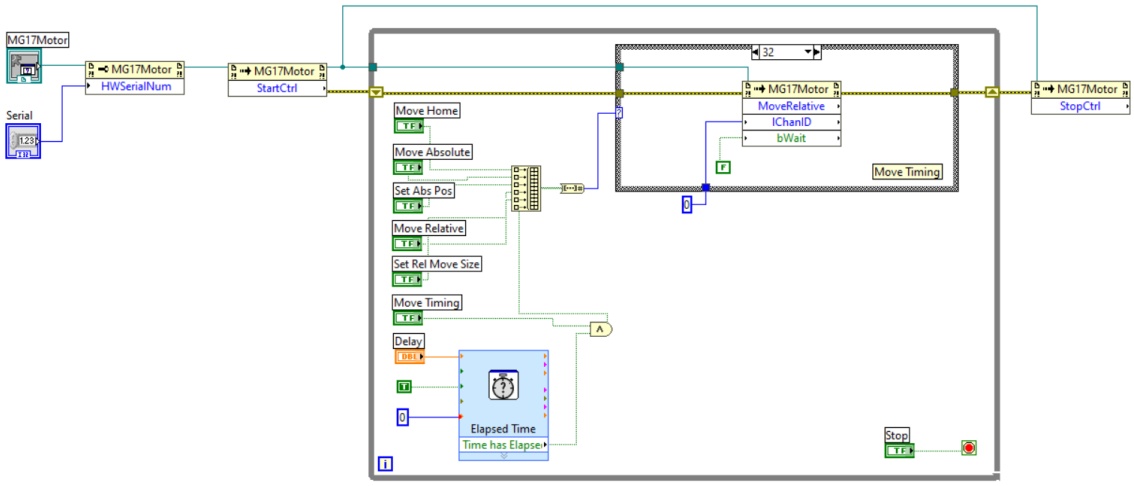

Figure 5.11: "Move Timing" block diagram

i.e. a node that subscribes to a topic does not know which node published the data.

Another way different nodes can communicate is by the use of services. The concept is similar to the topics but makes possible the request/reply interaction, which is not possible via the publish/subscribe interaction proposed by the topics. A node offers a named service, and a “client node” calls the service by sending the request message and awaiting the reply.

A message is a simple data structure, comprising typed fields. Standard primitive types (integer, floating point, Boolean, etc.) are supported, as are arrays of primitive types. Messages can include arbitrarily nested structures and arrays (much like C structs). Messages are exchanged by nodes by sending or reading it via topics and services.

During our work we found out that we could not use the infrared-light OCT and system and attach its sample arm in the robotic arm. Therefore, we did not program the movement of the robot in order to make its end effector, i.e. the device at the end of a robotic arm, move in a circular motion around an object. Nevertheless, we already had established a communication bridge between the OCT system and the robotic arm, by interfacing ROS and LabVIEW, which will be explained later in this section.

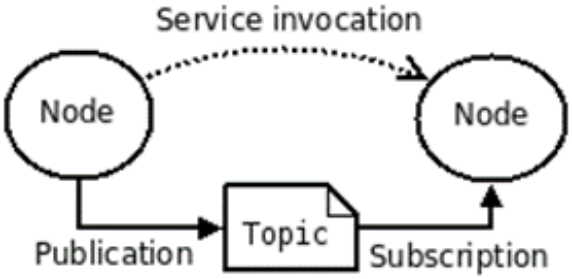

Figure 5.12: ROS basic concepts

5.4.4 Interfacing the OCT system and the rotational stage

The control of the OCT system and of the rational stage can be integrated into a single program in LabVIEW. Since we already managed to control before both the OCT system and the rational stage using LabVIEW, we only had to merge both programs into a single one and make some modifications. We added a new case "Move Stage", where we execute "MoveRelative" on the rotational stage. We also made some modifications to the saving process, by employing Stream channels instead of queues.

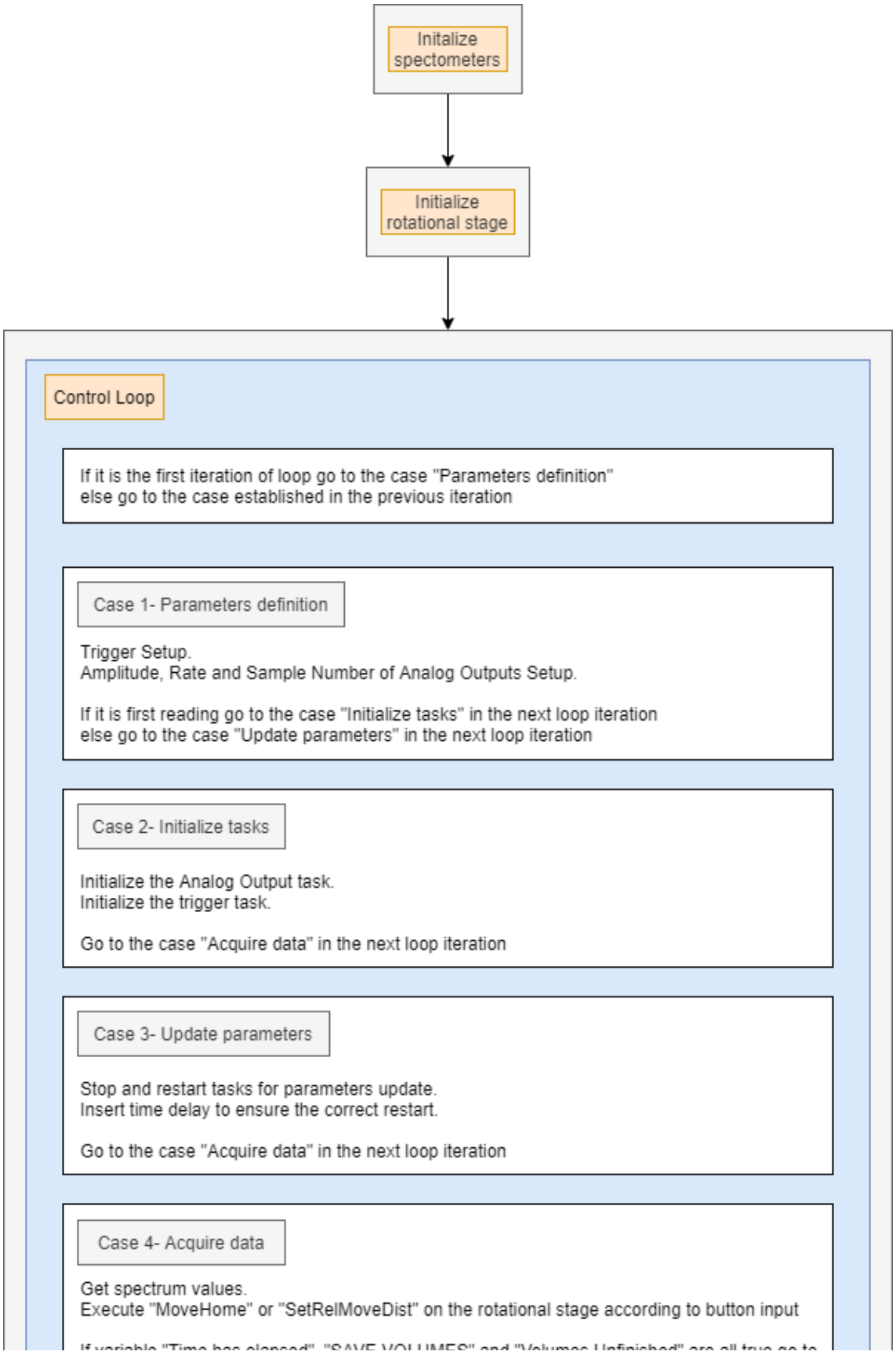

Figure 5.13: Control of OCT system and stage. Continues in next page.

Case 4- Acquire data

Get spectrum values.
Execute "MoveHome" or "SetRelMoveDist" on the rotational stage according to button input

If variable "Time has elapsed", "SAVE VOLUMES" and "Volumes Unfinished" are all true go to the case "Move Stage" in the next loop iteration
else
if variable "UPDATE" is true go to the case "Parameter definition" in the next loop iteration
else stays in the case "Acquire data" in the next loop iteration

Case 5- Move Stage

Execute "MoveRelative" on the rotational stage according to the "Rel Move Size".

Go to the case "Save 3D" in the next loop iteration

Case 6- Save 3D

The tasks are stop and restarted at a correct position.
Insert time delay to ensure the correct restart.

Go to the case "Acquire data" in the next loop iteration

Case 7- Stop

Stop taks before stopping execution to protect motor and camera
from abrupt voltage cut

Stays in the case "Stop" in the next loop iteration

If variable "STOP" is true go to the case "Stop" in the next loop iteration

Saving Loop

If variable "SAVE" is true
Set "FILE NAME" and "PATH TO SAVE".
Create the new file.
Read element from the Stream chanel and write the data to a file.
Close the file reference.

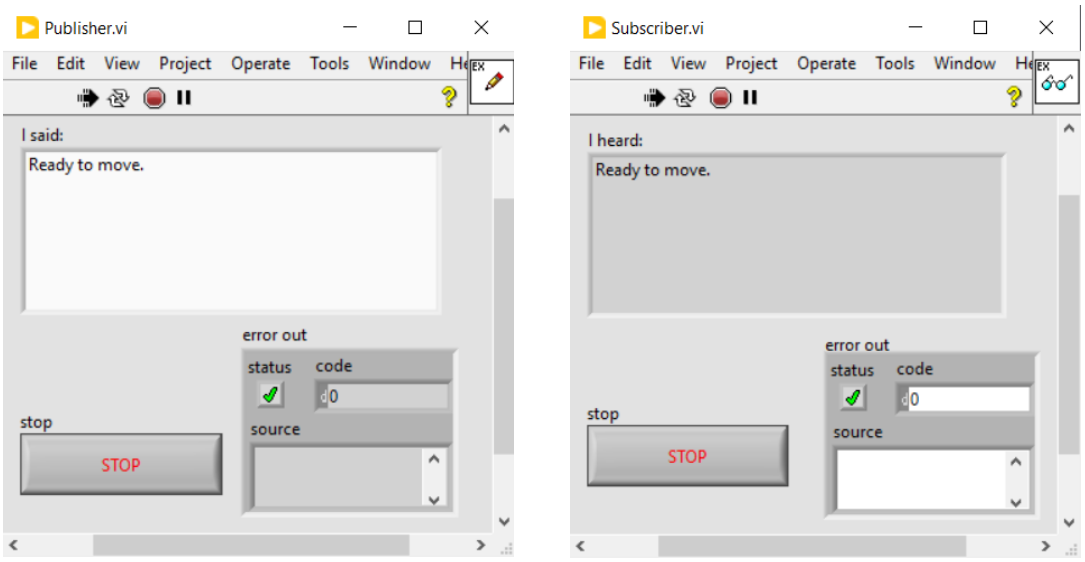

(a) Publisher front panel in LabVIEW (b) Subscriber front panel in LabVIEW

Figure 5.14: Publisher and subscriber front panel in LabVIEW

5.4.5 Interfacing the OCT system and the robotic arm

The interface between LabVIEW and ROS can be done using the ROSforLabVIEW package, a LabVIEW client API for communication with ROS applications [57]. With a set of VIs, it is possible to set up a connection to a Master (ROS), establish the communication between nodes using topics and services, and code or decode message strings.

Using TCP as the transport mechanism, the client library manages the node-to-node transport negotiation and communication setup. In addition, it also deals with transport specific serialization and deserialization of messages. Moreover, a sense of time can be introduced since the client library allows the subscription to a simulated clock.

To handle the communication between ROS nodes a master has to be set. We can either run this master on the Ubuntu computer running ROS or the windows computer running LabVIEW. Due to its simplicity, we ran it on Ubuntu, since we only have to run the command “roscore”. After that to establish the communication between the nodes running on LabVIEW and ROS, we need to set them as a subscriber or publisher to a topic. Since this communication has to be bilateral, we had to make sure that a subscriber in ROS can listen to a topic where a publisher in LabVIEW is sending information but also that subscriber in LabVIEW can receive information from a publisher in ROS. The publisher and subscriber front panel in LabVIEW are shown in Figure 5.14 a) and b), respectively. We can write a message to a topic on the Publisher.VI and it will be received by the nodes subscribed to that topic. In Figure 5.15, the block diagram for the publisher and subscriber are shown. Here we can define the topic and the message, among other parameters. For testing purposes, we used "/movement" as the topic and "String" as the message type.

The time delay between the sending of the message by the publisher and the receiving by the subscriber is around 1ms. This is not a problem since there is not a strict time constrain to

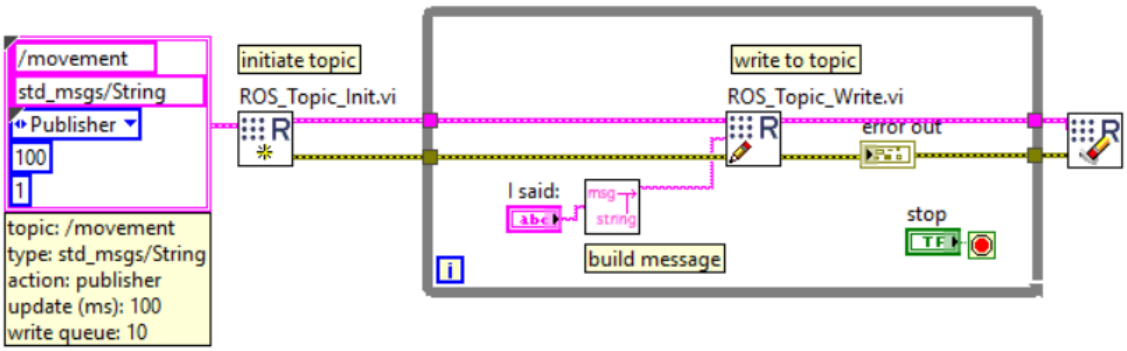

(a) Publisher block diagram in LabVIEW

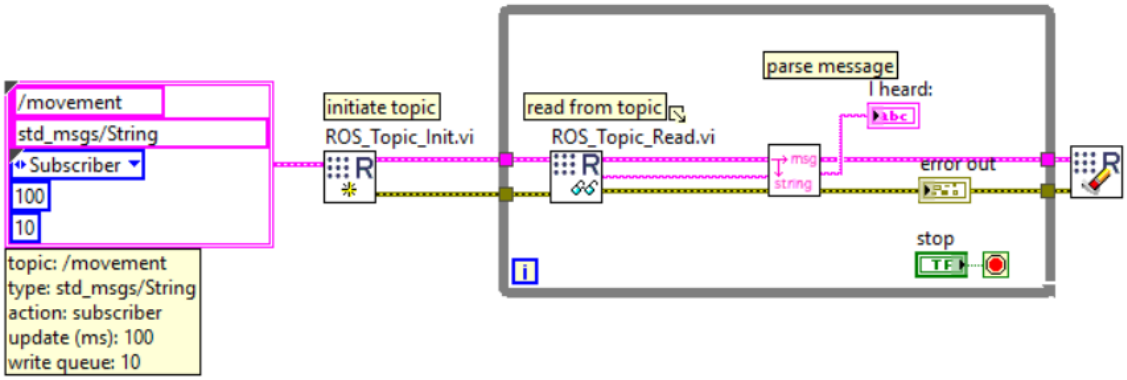

(b) Subscriber block diagram in LabVIEW

Figure 5.15: Publisher and subscriber block diagram in LabVIEW

exchange information between the robot and the OCT system.

Chapter 6

Automated stitching of OCT volumes

Most optical coherence tomography (OCT) imaging systems are limited by a relatively small field of view (FOV), with a magnitude of millimeters. Such FOV is inadequate to visualize the whole structure in various fields where this technology might be applied. Therefore, an increase of the FOV is highly desirable. Without additional changes to the current OCT system design, this can be achieved by stitching multiple overlapped OCT volumes into a single three-dimensional volume.

Volumetric stitching of OCT volumes is particularly challenging since the signal-to-noise ratio (SNR) in OCT images is very weak compared to other imaging modalities. As a result, the texture of the overlapped area in two overlapping volumes can differ, leading to a bad correlation and matching between volumes. Additionally, features extraction methods, like Scale-Invariant Feature Transform (SIFT) or Speeded Up Robust Features (SURF), are difficult to implement the extracted features may change as a consequence of noise and/or axial position of the sample [61]. Many existing stitching techniques for OCT volumes are implemented for medical and retinal imaging, where blood vessels constitute good features [51]. Additionally, these tissues often have layered structures, facilitating the registration in the depth direction. However, general approaches to stitch volumetric OCT data with methods suitable for applications outside the medical field are still scarce.

6.1 Proposed Framework

6.1.1 Setup and dataset

Three-dimensional volumetric data was obtained by imaging an object with a circular symmetry with the word 'thorlabs', which can be seen in the Figure 6.1. The data was acquired using the OCT system described in section 5. Using a rotational stage, we acquired in total five volumes with overlapping regions, rotating 5 degrees each time. We had to make sure that the overlapping area was big enough so we used a rotation of 5º on the rotational stage between each volume acquisition. In this experiment, each volume consists of $400 \times 2048 \times 400$ pixels, which translates to 4 x 1 x 4 mm in the x , z and y directions, respectively.

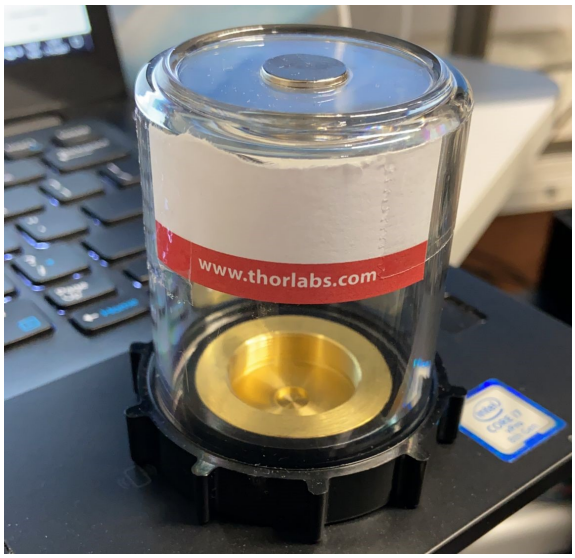

Figure 6.1: Circular object used to acquired the dataset

6.1.2 Implementation and algorithm flow

Our framework is implemented using MATLAB and its Image Processing Toolbox. To perform the stitching multiple OCT volumes, our algorithm consists of three main steps:

1. Volume pre-processing and denoising
2. Denoising and binarization of en face images
3. Volume registration - template matching
4. Volume blending and stitching

In step 1, the original OCT volume is properly denoised, making it adequate for the registration process in the next step. In step 2, the image projection of each volume is computed and denoising and binarization methods are applied to each image. In step 3, the translation in x and y between two consecutive volumes is estimated, using a denoised binary image projection of each volume. Finally, in step 4, the volumes are stitched together and seamless blended.

6.1.3 Step 1: Volume pre-processing and denoising

The original 3D OCT images are expressed as a 400 x 2048 x 400 matrix, with the first, middle and last dimensions corresponding to x, z and y dimensions respectively. This means that each A-scan has 2048 values, each B-scan consists of 400 A-scans, and each 3D OCT volume consists of 400 B-scans. Before applying further pre-processing techniques, we converted the matrix to a grayscale image, returned as a numeric matrix with values in the range [0,1].

Pre-processing starts by extracting cross-sectional B-scan images from the acquired 3D OCT images. Due to the OCT imaging properties, we opted to only consider the values between 50 and

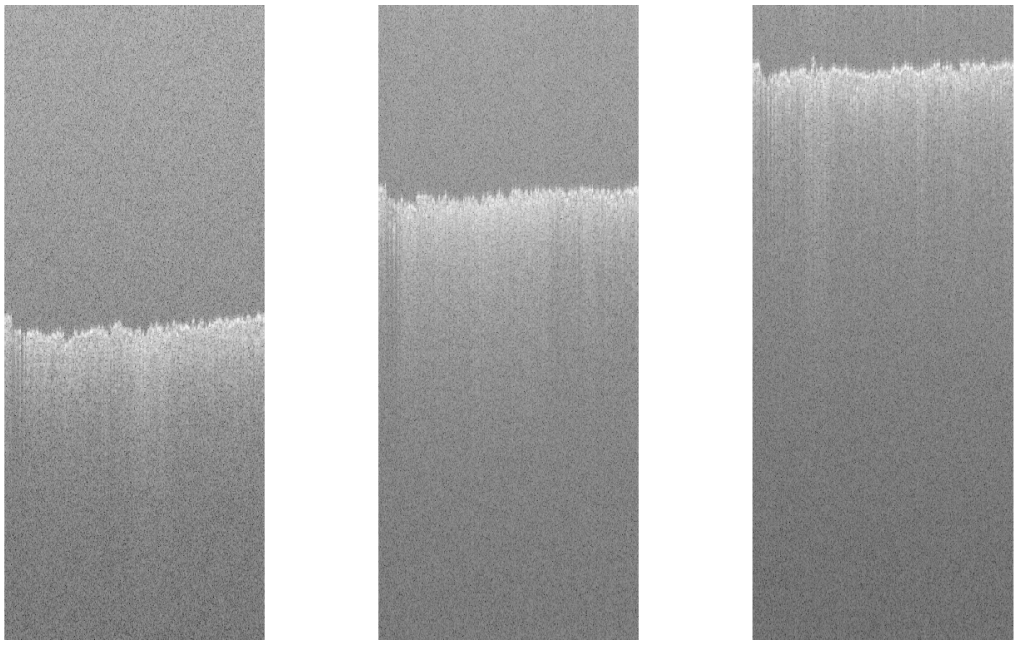

(a) B-scan at position x=1 (b) B-scan at position x=150 (c) B-scan at position x=350

Figure 6.2: Original B-scans of the volume acquired at 0º

1024 for each A-scan, resulting in B-scans images of size 400x975. From the input volume vol, the B-scan at the position i is given by:

$$bscan_i = 10 * \log_{10}(squeeze(vol(i, 50 : end/2, :))); \tag{6.1}$$

The original b-scans at the positions 1, 150 and 350 of the volume acquired at the position 0º, without any filtering, are shown in Figure 6.2.

As we can see, the image has a lot of noise, leading to a low signal-to-noise ratio. To improve the quality of the image and increase the signal-to-noise ratio we tested two common denoising filters on B-scan images.

One of the tested filter was the 2-D median filter, which was applied to each B-scan image to reduce the speckle noise, via the medfilt2 function. We chose this filter because it has a good performance in reducing the effects from small, discrete but strong noise, which is the case of the speckle noise. Using a m x n window size, in the output image, each pixel contains the median value in a m-by-n neighborhood around the corresponding pixel in the input image.

The other tested filter was the adaptive 2-D Wiener filter, which was applied to each B-scan image to reduce additive random noise, via the wiener2 function. We chose this filter because it was reported to have a good performance in suppressing speckle noise. This filter computes estimate the local image mean and standard deviation around each pixel, according to the given size of the neighborhood [62]. Using these estimates, wiener2 then creates a Wiener filter for each pixel. The higher the variance, the less smoothing wiener2 performs.

For both filters, we denoised the OCT volume using three sizes for the neighborhood, [3 3], [5

5] and [7 7]. After that we computed the SNR of each denoised volume by averaging the SNR of its B-scans, which can be obtained by averaging the SNR of its A-scans. The SNR formula that we used was:

$$SNR_{dB} = 10\log_{10}(\frac{I_{max}^2}{\sigma_{noise}^2}) \tag{6.2}$$

where I_{max} is the maximum intensity of the A-scan and σ_{noise} is standard deviation of the noise. From the Figure 6.3, we can see intensity signal and noise background in a OCT depth profile. For work, we computed the standard deviation of the noise as:

$$\sigma_{noise}^2 = \frac{1}{N}\sum_{i=1}^{N}(I_i - \mu)^2 \tag{6.3}$$

where, I_i is the intensity of the noise at position i and μ is the mean noise. We calculated the value of standard deviation of the noise for the range of depth before the imaging surface, namely between 50 and 100.

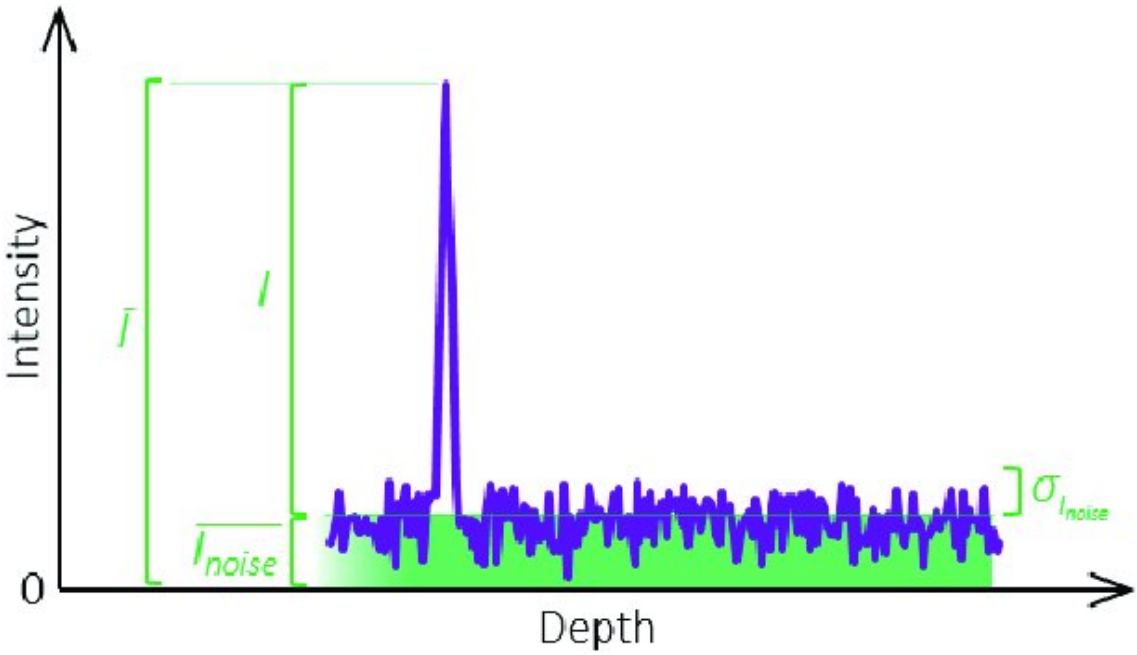

Figure 6.3: Intensity signal and noise floor in a schematic OCT depth profile [8]

In the Table 6.1 we can see a comparison of the performance of the filters used. The original OCT volume had a SNR equal to 37.122dB. As we can observe the adaptive wiener filter performs better than the median for every window size. Note that larger window sizes lead to more noise reduction but also introduce more blurring. Therefore, We opted for the adaptive wiener filter with neighborhood size [5 5] since it gives a good compromise between noise reduction and non-blurring. The filtered b-scans using the median filter can be seen in Figure 6.4. The filtered b-scans using the wiener filter can be seen in Figure 6.5.

SNR of the OCT volumes after filtering			
Filter	window [3 3]	window [5 5]	window [7 7]
Median	40.823 dB	41.974 dB	42.845 dB
Adaptive Wiener	40.879 dB	43.145 dB	44.470 dB

Table 6.1: SNR of the OCT volumes after filtering

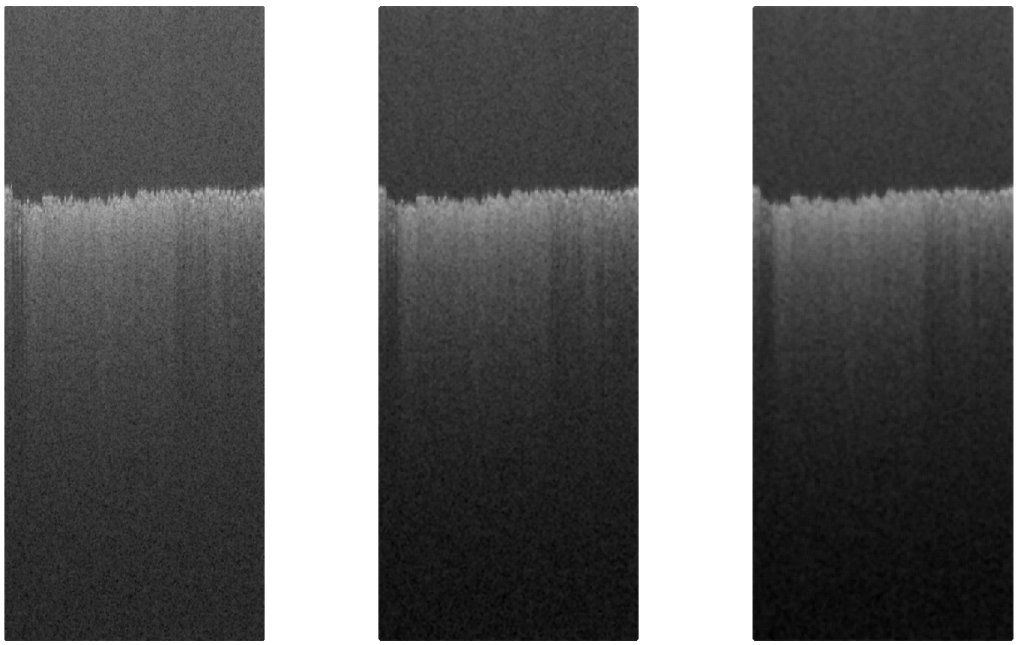

(a) Windows size [3 3] (b) Windows size [5 5] (c) Windows size [7 7]

Figure 6.4: B-scans at the position x=150 of the volume acquired at 0º filtered using an median filter

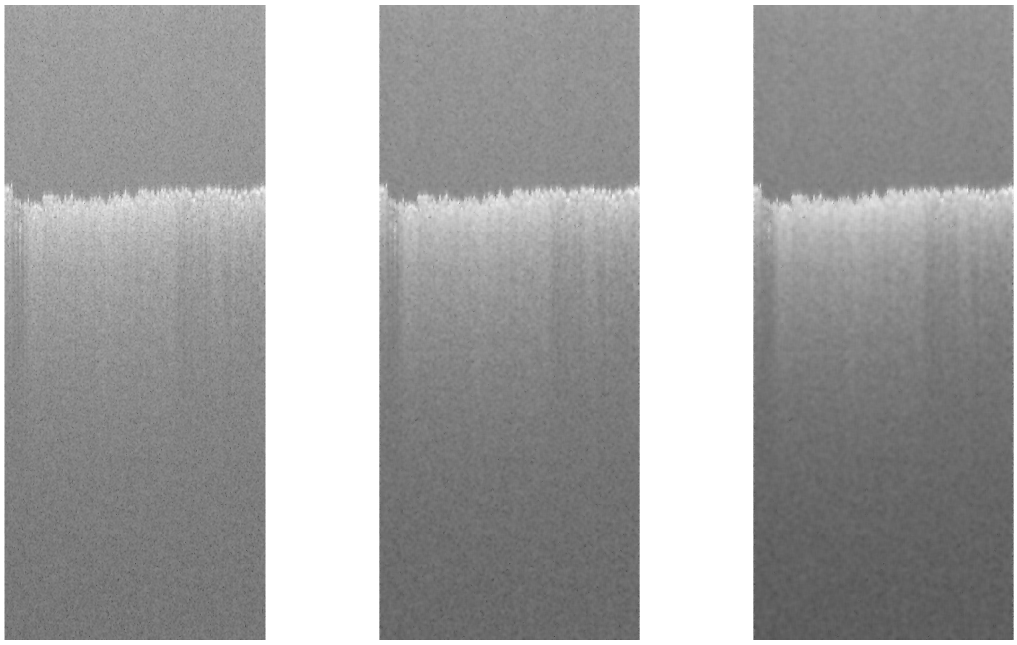

(a) Windows size [3 3] (b) Windows size [5 5] (c) Windows size [7 7]

Figure 6.5: B-scans at the position x=150 of the volume acquired at º0 filtered using an adaptive wiener filter

To further verify the effectiveness of this adaptive wiener filter with neighborhood size [5 5], from the previously denoised OCT volume, a 2D projection of the volume was created using the summed-voxel projection (SVP) method. By summing all pixel values along the axial lines, an image displaying the imaging surface en face is generated.

Then a scaling of the gray limits is done so that the full range [0 1] is used in the image. The scaled image I_{scaled} is given by:

$$I_{scaled} = \frac{I - I_{min}}{I_{max} - I_{min}} \tag{6.4}$$

where I is the input image and I_{max} and I_{min} are the maximum value and minimum value in the image I, respectively.

The image projection of the filtered volume was compared with the image projection the original volume, without any pre-processing. Both images are shown in Figure 6.6. As we can observe, the en face image after filtering is a lot smoother and its noise seems to have been reduced.

6.1.4 Step 2: Denoising and binarization of en face images

After denoising all the volumes from the dataset using the adaptive wiener filter with neighborhood size [5 5], the next step is the registration of consecutive volumes. Even though the overall signal-to-noise ratio of the these volumes was significantly improved, it still falls behind the values

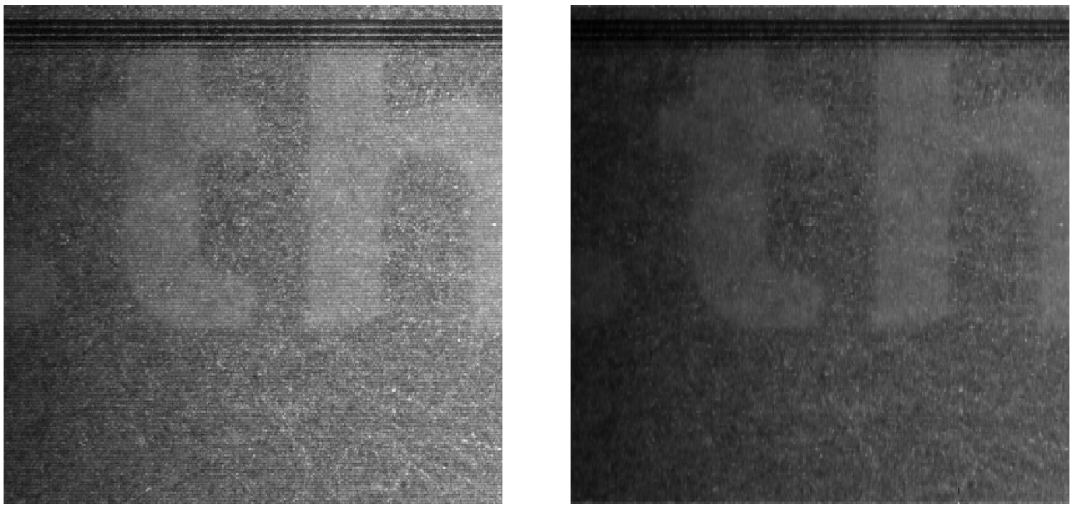

(a) Before applying any filtering (b) After applying the adaptive wiener filter

Figure 6.6: Image projections of the volume acquired at º0, before and after applying the adaptive wiener filter

obtained by other imaging modalities, like computed tomography and magnetic resonance imaging. For a optimal registration process, both volumes have to possess equivalent features, that should be uniformly distributed across the entire volume and consistent over time.

Since the features within en face images are a more reliable reference for registration than the features within the volume data, we based our algorithm on the registrations of en face images. Before estimating the offset between two consecutive en face images, we applied multiple image pre-processing and denoising techniques to the enface images. We utilized the denoised binary en face images as inputs for the registration process.

In order to get better results on the registration process the en face images have to be denoised and binarized. By making the main image features more predominant, the correlation between the same object in two different images will be higher.

The intensity levels across the OCT volume in one or more directions can vary quite a lot. As a result, the intensity levels across the respective en face image can also have some changes. As we can see in Figure 6.6, this is our case. This occurs because the rotation axis of the object placed in the rotational stage is different than the rotation axis of the rotational stage itself, introducing some variations in the depth of focus of the imaging lens. To deal with this problem, one possible approach is to divided the image in question by a extremely blurred version of itself. To get this blurred image, using the function imgaussfilt, we filtered the scaled image with a 2D Gaussian smoothing kernel with standard deviation of 50. Then, an uniformization of intensity levels was achieved by dividing each pixel in the scaled image by its counterpart in the blurred image. : Two consecutive en face images after intensity levels uniformization can be seen in Figure 6.7.

Later, the block matching and 3D filtering (BM3D) method was applied to to denoise the en face image with uniform intensity levels and enhance the boundaries. This advanced denoising technique can be considered a collaborative filtering approach that combines sliding-window

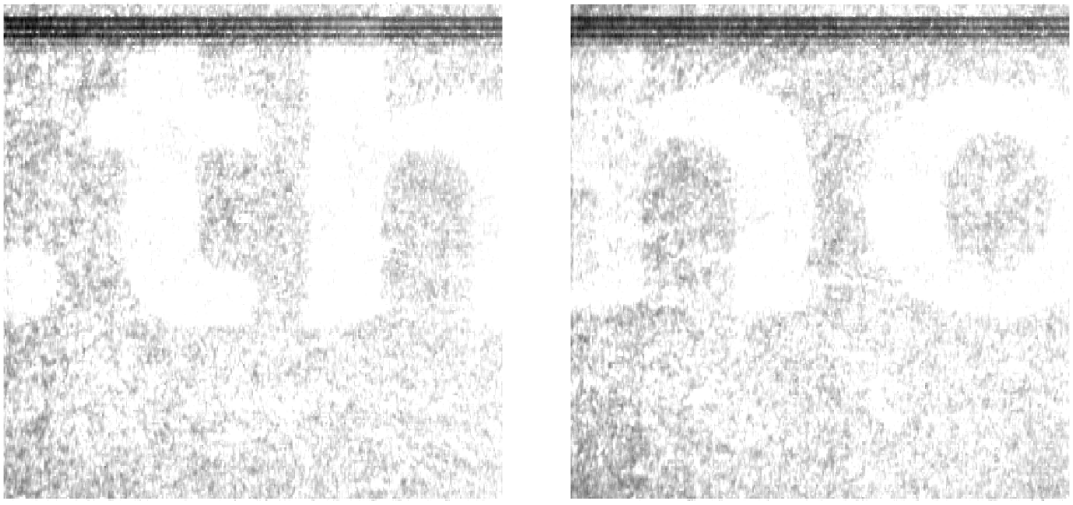

(a) (b)

Figure 6.7: En face images of the volume acquired at 0º a) and 5º b) after intensity levels uniformization

transform processing with block-matching [63]. Succinctly, the BM3D algorithm groups similar 2D image patches in multiple 3D block and filters at once all 2D image patches in each 3D block. This method was implemented using a custom made function BM3D, where the standard deviation the noise was set to 5. This filter was able to significantly supress noise in the enface image, as shown in Figure 6.8.

From the denoised en face image, using the function edge, we generated a binary image with 1s where the function finds edges in the image and 0s elsewhere. This function looks for locations in the image where the intensity changes abruptly, which are often associated with the boundaries of objects. The edge-detection algorithm used was 'log', which finds edges by looking for zero-crossings after filtering the image with a Laplacian of Gaussian (LoG) filter. The resulting binary en face image with well defined edges can be been in Figure 6.9.

The binary en face image obtained through the edge detection function gives us the overall shape of the most predominant features, letters in this case, However the background is not uniform and consists on a cluster of points, small lines and disks. Therefore, in order to homogenize the background for all images, we performed a set of morphological operations, such as dilation, opening and area opening. These operations were done in order to not only remove small insignificant objects but also fill the holes in big objects, while preserving their size and general shape.

The two first and most important operations were the dilation and the area opening. The former is applied to increase the size of the elements in the background, using the function imdilate. Since most of the elements in the background have the shape of a disk, we chose a disk-shaped structuring element, with a radius equal to 4. This value was chosen so the background is more or less without compromising the shape of the main features. The resulting image for two different volumes can be seen in Figure 6.10. Subsequently, after inverting the image, we performed an area

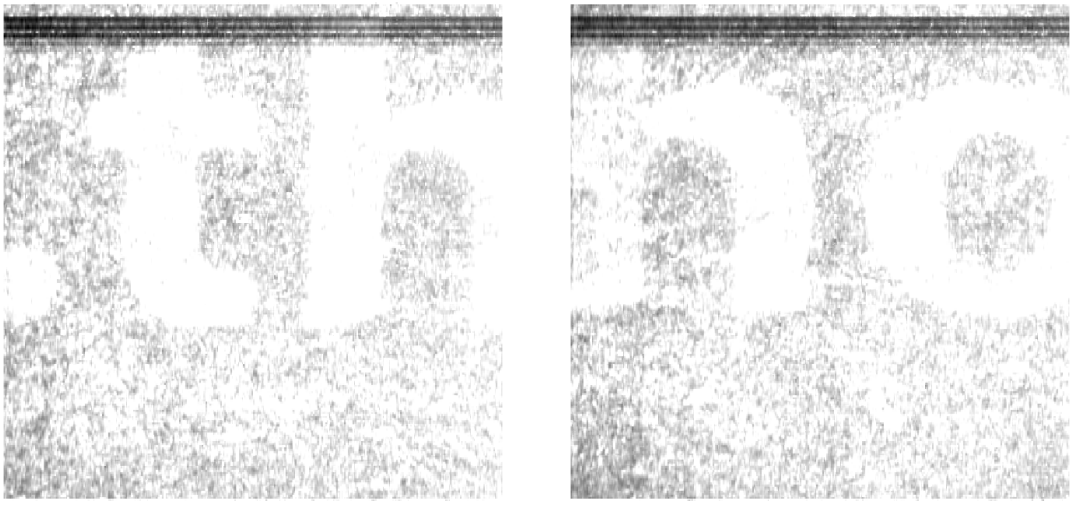

(a) (b)

Figure 6.8: En face images of the volume acquired at 0º a) and 5º b) after applying B3MD filter

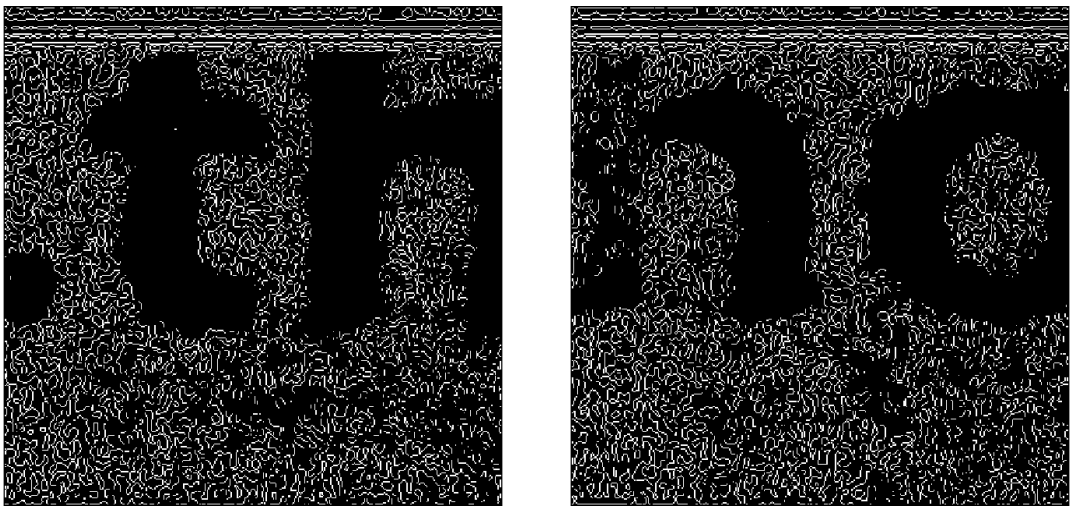

(a) (b)

Figure 6.9: En face images of the volume acquired at 0º a) and 5º b) with edges determined

(a) (b)

Figure 6.10: En face images of the volume acquired at 0º a) and 5º b) after dilation

opening to remove the remaining small objects in the background or even in the main features. This was done using the function bwareaopen, and we removed every components with less than 1500 pixels. The resulting image for two different volumes can be seen in Figure 6.11.

With these two operations, the binary en face image already has seen major improvements. However there might be still some holes in the main objects. Therefore, we wrote a function fill_small_holes to cover only the small object in the image. First, we compute a filled image by filling all holes using the function imfill. Then, we compute a holes image by identify the pixels which constitute holes, using logical operators on the filled and original images. The third step is to use the area opening operation on the holes image to eliminate small holes. Finally, using logical operators to identify the small holes we can fill in only the small holes in the original image. The resulting images for two different volumes can be seen in Figure 6.12.

Finally, we perform a opening operation, using the imopen function with a disk-shaped structuring element, with a radius equal to 1. This is done to separate small noisy objects from the main objects and smooth the rough edges. The resulting images for two different volumes can be seen in Figure 6.13. The separated noisy objects are removed from the image using the area opening operation. The final binary images for two different volumes can be seen in Figure 6.14.

6.1.5 Step 3: Volume registration - template matching

The registration of two consecutive OCT volumes is done using their respective filtered binary en face images. A template-matching approach was employed, where we used the normalized cross-correlation method to find the correlation between the image and the template for each possible position of the template. The position for which the normalized cross-correlation has the highest value denotes the optimal registration between the template and the image.

(a) (b)

Figure 6.11: En face images of the volume acquired at 0º a) and 5º b) after area opening

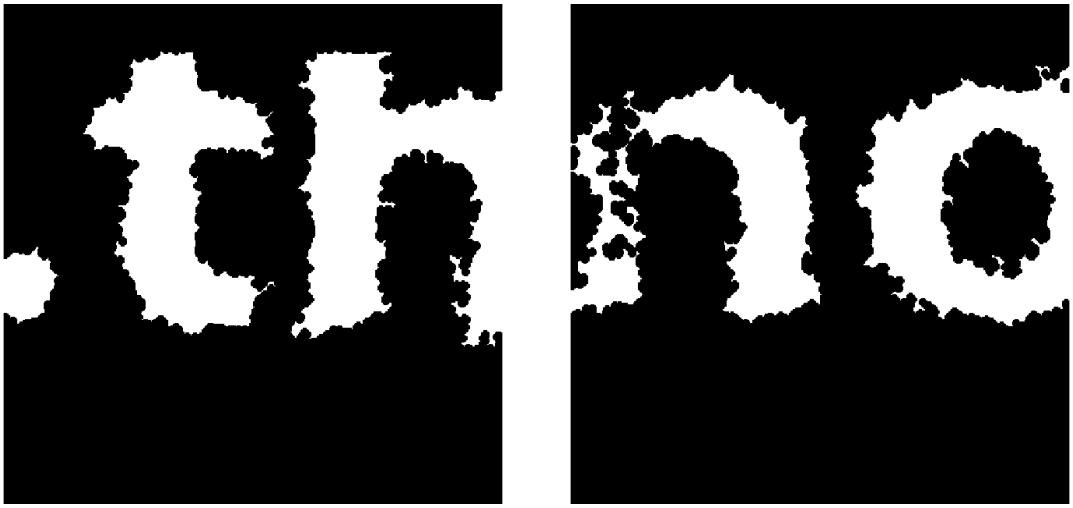

(a) (b)

Figure 6.12: En face images with small hole filled

(a) (b)

Figure 6.13: En face images after opening

(a) (b)

Figure 6.14: Final binary en face images

(a) (b)

Figure 6.15: Final en face images for volumes acquired at 0º and 5º

Given two consecutive binary en face images we assume that there is an overlapping area between them. Additionally, we start from the premise that on the first image, this overlapping area is situated on its right side because the rotation of the rotation stage was clock-wise. Therefore, we define the template image as a windows on the right side of the first image and the reference image as the second image.

The correlation map is computed using the normxcorr2_general function, providing the template image and the reference image as inputs. The peak of the cross-correlation matrix occurs where the two images are best correlated. Thus, the optimal translation values in the x and y directions depends on the location of the peak in the correlation map, and on the size and position of the template image.

For the registration of the two consecutive volumes, we take their filtered binary en face images obtained in the previous step. Two pair of consecutive en face images is shown on Figure 6.15 and Figure 6.16.

The respective template for each normalized cross-correlation computation is shown on Figure 6.17.

The respective correlation map for each normalized cross-correlation computation is shown on Figure 6.18.

To better view the correlation between the template and the highest correlated area in the reference image, the matched area for each normalized cross-correlation computation is shown on Figure 6.19.

6.1.6 Step 3: Volume blending and stitching

The stitched volume is obtained by combining the multiple volumes into one single volume, using the translation values determined in the previous step. Ideally, when performing image stitch-

(a) (b)

Figure 6.16: Final en face images for volumes acquired at 10º and 15º

(a) (b)

Figure 6.17: Template images for two different normalized cross-correlation computation

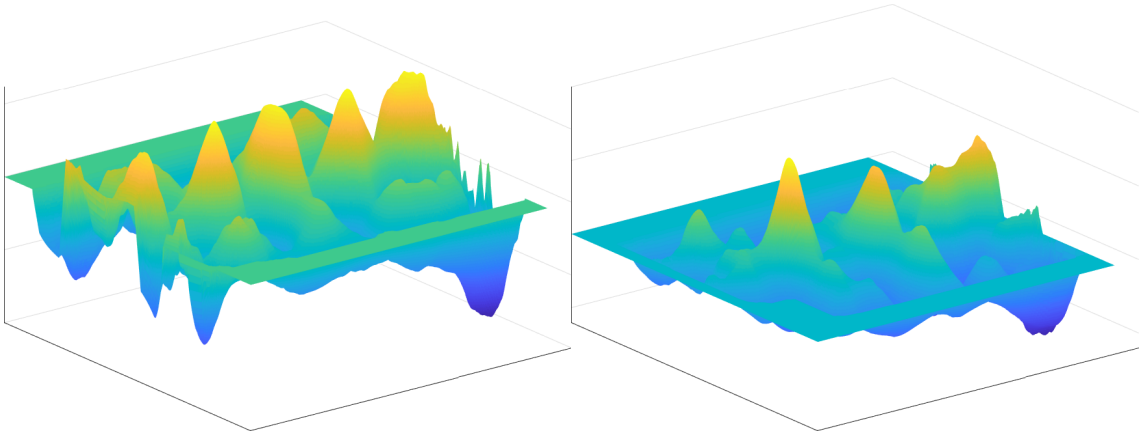

(a) (b)

Figure 6.18: Correlation map for two different normalized cross-correlation computations

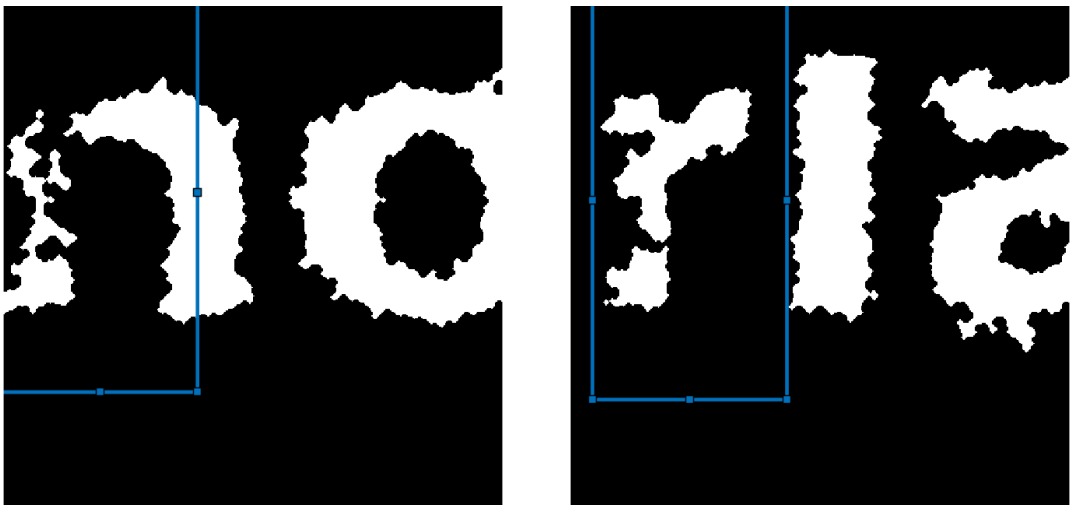

(a) (b)

Figure 6.19: Matching area for two different normalized cross-correlation computations

ing, in the overlapped region, the voxel values of both volumes should be the same. However, usually this is not the case, with the contrast in overlapped region varying a lot across multiple volumes. Therefore, there is a visible edge in the stitched volume. To deal with this problem, we implemented a blending procedure using two different methods

On the first methods, the final stitched volume is computed so that the final voxel intensity in the overlapping region is the mean of two overlapping intensities. An image projection of this stitched volume is shown in Figure 6.20.

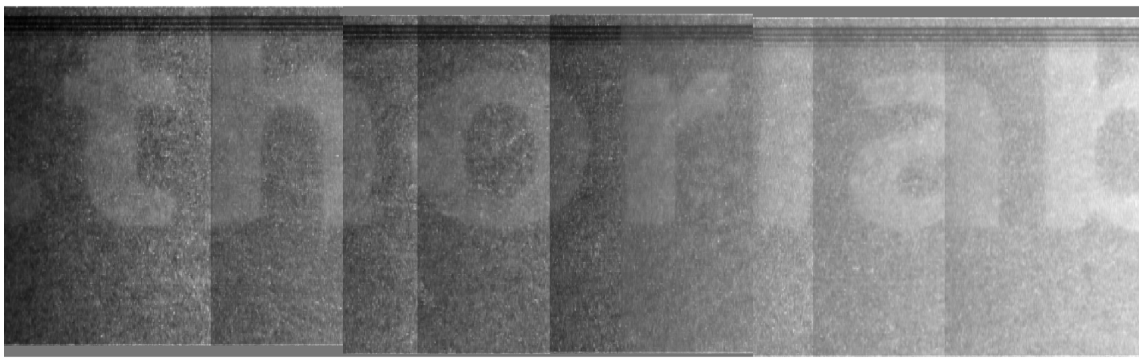

Figure 6.20: Stitched volume blending method 1

On the second methods, described in more detail previously, the final stitched volume is computed so that the final voxel intensity in the overlapping region considers not only the intensity of two overlapping intensities but also the distance of the pixel to the non overlapping area in each volume. An image projection of this stitched volume is shown in Figure 6.21.

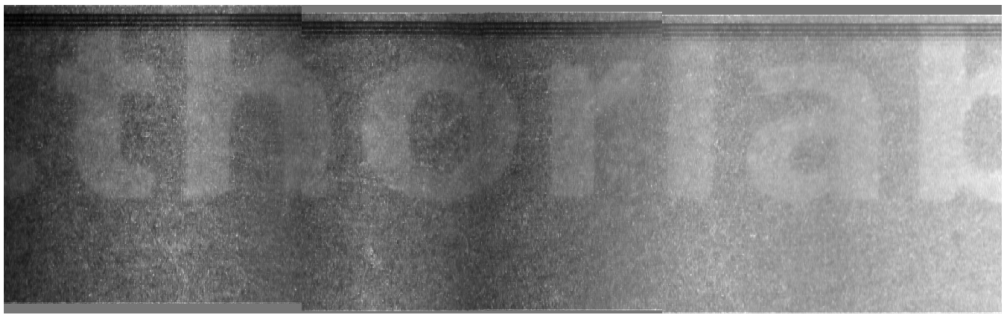

Figure 6.21: Stitched volume blending method 2

6.2 Analysis of results and discussion

Here we will analyze the results obtained after applying our stitching algorithm to the dataset in question. Then, we will discuss the work done and some of the drawbacks faced during the project and ways to improve.

We present a framework to stitch multiple overlapping OCT volumes with the goal of increasing the field of view of image scanning. The algorithm is validated on OCT data collected from an object with a circular geometry. Analyzing the stitched volume using the first blending method and the stitched volume using the second blending method we can observe that in both of them the overall stitching position was correct. However the second method does a much better job at stitching the overlapping areas, since it has almost no visible seams or sharp edges. The implemented blending method was able to enhance the visualization of stitched data. In general, this generic method allows an expanded FOV for image analysis. Without requiring any hardware changes to the OCT system, the enlarged FOV should be of great benefit to various OCT imaging applications.

We believe that the proposed framework can work with a variety of dataset. The main focus of preoccupation regarding its use with other datasets resides in step 2.1: Denoising and binarization of en face images. Since in different OCT volumes the size and shape of predominant features might vary, the operations performed during this step may suppress them. Another concern is also the filtering of the speckle noise which may also be inconsistent. However, we are convinced that the operations performed and the parameters used are general enough to adapt to a wide range of datasets.

Due to some technical problems with the OCT system, we were not able to quantify and measure the performance of our framework. However we suggest to replicate the acquisition of the current dataset but rotating the stage 2.5 degrees each time, leading to 9 OCT volumes in total. Then, we can evaluate the performance of this algorithm by computing the normalized cross-correlation between the volumes acquired at the new position and the previously stitched volume. If the degree of similarity is high enough we can conclude that our algorithm was successful.

Chapter 7

Conclusion and future work

7.1 Future work

In the future, we can examine the Phase Correlation method to perform the registration of the overlapping OCT volumes. Also, the implementation of this framework in a GPU can be explored to increase the speed of the registration process, compared to the current CPU implementation. Furthermore, the implementation for multiple GPUs is also to be considered. The faster registration time allows the stitching algorithm suitable for real-time applications.

7.2 Conclusion

In conclusion, this thesis presented an automatic registration method to stitch multiple OCT volumes. With various techniques such as image-pre processing, template-matching and image blending we achieved a good registration accuracy, enabling a high-resolution, high-density OCT imaging with macro-view. By showing a large view of a circular object with distinct characteristics for validation, we displayed our algorithm's capacity in automatic stitching. The imaging system allows 3D reconstruction of materials for Non-destructive testing and potentially art works or other cultural heritage objects.

Bibliography

[1] A. Baghaie, R. D'souza, and Z. Yu, "Sparse And Low Rank Decomposition Based Batch Image Alignment for Speckle Reduction of retinal OCT Images," vol. 2015, Nov. 2014.

[2] D. P. Popescu, L.-P. Choo-Smith, C. Flueraru, Y. Mao, S. Chang, J. Disano, S. Sherif, and M. G. Sowa, "Optical coherence tomography: Fundamental principles, instrumental designs and biomedical applications," *Biophysical Reviews*, vol. 3, no. 3, p. 155, Aug. 2011. [Online]. Available: https://doi.org/10.1007/s12551-011-0054-7

[3] J. A. Izatt and M. A. Choma, "Theory of Optical Coherence Tomography," in *Optical Coherence Tomography: Technology and Applications*, ser. Biological and Medical Physics, Biomedical Engineering, W. Drexler and J. G. Fujimoto, Eds. Berlin, Heidelberg: Springer, 2008, pp. 47–72. [Online]. Available: https://doi.org/10.1007/978-3-540-77550-8_2

[4] A. Baghaie, R. D'souza, and Z. Yu, "State-of-the-Art in Retinal Optical Coherence Tomography Image Analysis," *Quantitative Imaging in Medicine and Surgery*, vol. 5, pp. 603–617, Aug. 2015.

[5] T. B. Moeslund, *Introduction to Video and Image Processing: Building Real Systems and Applications*, ser. Undergraduate Topics in Computer Science. London: Springer-Verlag, 2012. [Online]. Available: https://www.springer.com/gp/book/9781447125020

[6] C. Zhao, C. Cheung, and M. Liu, "Integrated polar microstructure and template-matching method for optical position measurement," *Optics Express*, vol. 26, no. 4, pp. 4330–4345, Feb. 2018.

[7] "Three-dimensional spectral measurements of paint samples using optical coherence tomography." [Online]. Available: https://www.spiedigitallibrary.org/conference-proceedings-of-spie/11784/117840Q/Three-dimensional-spectral-measurements-of-paint-samples-using-optical-coherence/10.1117/12.2592663.short?SSO=1

[8] B. Baumann, C. W. Merkle, R. A. Leitgeb, M. Augustin, A. Wartak, M. Pircher, and C. K. Hitzenberger, "Signal averaging improves signal-to-noise in OCT images: But which approach works best, and when?" *Biomedical Optics Express*, vol. 10, no. 11,

pp. 5755–5775, Oct. 2019. [Online]. Available: https://www.ncbi.nlm.nih.gov/pmc/articles/PMC6865101/

[9] S. K. Dwivedi, M. Vishwakarma, and P. A. Soni, "Advances and Researches on Non Destructive Testing: A Review," *Materials Today: Proceedings*, vol. 5, no. 2, Part 1, pp. 3690–3698, Jan. 2018. [Online]. Available: https://www.sciencedirect.com/science/article/pii/S2214785317328936

[10] "Introduction to Nondestructive Testing." [Online]. Available: https://www.asnt.org/MajorSiteSections/About/Introduction_to_Nondestructive_Testing.aspx

[11] F. SA, "NDT (Non-Destructive Testing): What It Is, Common Methods & Industries, and How Drones Can Help." [Online]. Available: https://www.flyability.com/ndt

[12] B. J. Rouba, P. Karaszkiewicz, and L. Tymi, "Optical Coherence Tomography for Non-Destructive Investigations of Structure of Objects of Art," p. 10.

[13] "Optical Coherence Tomography – Applications in Non- Destructive Testing and Evaluation | IntechOpen." [Online]. Available: https://www.intechopen.com/chapters/43475

[14] L. Dingemans, V. Papadakis, P. Liu, A. Adam, and R. Groves, *Optical Coherence Tomography Complemented by Hyperspectral Imaging for the Study of Protective Wood Coatings*, Jun. 2015, vol. 9527.

[15] F. Zechel, R. Kunze, N. König, and R. H. Schmitt, "Optical coherence tomography for non-destructive testing," *tm - Technisches Messen*, vol. 87, no. 6, pp. 404–413, Jun. 2020. [Online]. Available: https://www.degruyter.com/document/doi/10.1515/teme-2019-0098/html

[16] "Multi-reference global registration of individual A-lines in adaptive optics optical coherence tomography retinal images." [Online]. Available: https://www.spiedigitallibrary.org/journals/journal-of-biomedical-optics/volume-26/issue-01/016001/Multi-reference-global-registration-of-individual-A-lines-in-adaptive/10.1117/1.JBO.26.1.016001.full

[17] M. Finke, S. Kantelhardt, A. Schlaefer, R. Bruder, E. Lankenau, A. Giese, and A. Schweikard, "Automatic scanning of large tissue areas in neurosurgery using optical coherence tomography," *The international journal of medical robotics + computer assisted surgery: MRCAS*, vol. 8, no. 3, pp. 327–336, Sep. 2012.

[18] M. Niemeijer, K. Lee, M. K. Garvin, M. D. Abràmoff, and M. Sonka, "Registration of 3D spectral OCT volumes combining ICP with a graph-based approach," in *Medical Imaging 2012: Image Processing*, vol. 8314. SPIE, Feb. 2012, pp. 378–386. [Online]. Available: https://www.spiedigitallibrary.org/conference-proceedings-of-spie/8314/83141A/Registration-of-3D-spectral-OCT-volumes-combining-ICP-with-a/.full

[19] N. A. Kharousi, U. K. Wali, and S. Azeem, *Current Applications of Optical Coherence Tomography in Ophthalmology*. IntechOpen, Mar. 2013. [Online]. Available: https://www.intechopen.com/chapters/43462

[20] J. Fujimoto and W. Drexler, "Introduction to Optical Coherence Tomography," in *Optical Coherence Tomography: Technology and Applications*, ser. Biological and Medical Physics, Biomedical Engineering, W. Drexler and J. G. Fujimoto, Eds. Berlin, Heidelberg: Springer, 2008, pp. 1–45. [Online]. Available: https://doi.org/10.1007/978-3-540-77550-8_1

[21] Y. Baran, K. Rabenorosoa, G. J. Laurent, P. Rougeot, N. Andreff, and B. Tamadazte, "Preliminary results on OCT-based position control of a concentric tube robot," in *2017 IEEE/RSJ International Conference on Intelligent Robots and Systems (IROS)*, Sep. 2017, pp. 3000–3005.

[22] U. Sharma, E. W. Chang, and S. H. Yun, "Long-wavelength optical coherence tomography at 1.7 *M*m for enhanced imaging depth," *Optics express*, vol. 16, no. 24, pp. 19 712–19 723, Nov. 2008. [Online]. Available: https://www.ncbi.nlm.nih.gov/pmc/articles/PMC2773451/

[23] "Optical coherence tomography: A review of clinical development from bench to bedside." [Online]. Available: https://www.spiedigitallibrary.org/journals/Optical-coherence-tomography--a-review-of-clinical-development-from/volume-12/issue-05/051403/Optical-coherence-tomography--a-review-of-clinical-development-from/10.1117/1.2793736.full?SSO=1

[24] "A powerful new tool for medical imaging and industrial measurement." [Online]. Available: https://spie.org/news/0874-a-powerful-new-tool-for-medical-imaging-and-industrial-measurement

[25] S. Radhakrishnan, J. Goldsmith, D. Huang, V. Westphal, D. K. Dueker, A. M. Rollins, J. A. Izatt, and S. D. Smith, "Comparison of Optical Coherence Tomography and Ultrasound Biomicroscopy for Detection of Narrow Anterior Chamber Angles," *Archives of Ophthalmology*, vol. 123, no. 8, pp. 1053–1059, Aug. 2005. [Online]. Available: https://doi.org/10.1001/archopht.123.8.1053

[26] S. Aumann, S. Donner, J. Fischer, and F. Müller, "Optical Coherence Tomography (OCT): Principle and Technical Realization," in *High Resolution Imaging in Microscopy and Ophthalmology: New Frontiers in Biomedical Optics*, J. F. Bille, Ed. Cham: Springer International Publishing, 2019, pp. 59–85. [Online]. Available: https://doi.org/10.1007/978-3-030-16638-0_3

[27] R. B. Rosen, P. Garcia, A. G. Podoleanu, R. Cucu, G. Dobre, M. E. J. van Velthoven, M. D. de Smet, J. A. Rogers, M. Hathaway, J. Pedro, and R. Weitz, "En-Face Flying Spot OCT/Ophthalmoscope," in *Optical Coherence Tomography: Technology and Applications*, ser. Biological and Medical Physics, Biomedical Engineering, W. Drexler and J. G.

Fujimoto, Eds. Berlin, Heidelberg: Springer, 2008, pp. 447–474. [Online]. Available: https://doi.org/10.1007/978-3-540-77550-8_15

[28] A. Dubois and A. C. Boccara, "Full-Field Optical Coherence Tomography," in *Optical Coherence Tomography: Technology and Applications*, ser. Biological and Medical Physics, Biomedical Engineering, W. Drexler and J. G. Fujimoto, Eds. Berlin, Heidelberg: Springer, 2008, pp. 565–591. [Online]. Available: https://doi.org/10.1007/978-3-540-77550-8_19

[29] J. F. de Boer, C. K. Hitzenberger, and Y. Yasuno, "Polarization sensitive optical coherence tomography – a review [Invited]," *Biomedical Optics Express*, vol. 8, no. 3, pp. 1838–1873, Feb. 2017. [Online]. Available: https://www.ncbi.nlm.nih.gov/pmc/articles/PMC5480584/

[30] R. Hamdan, R. G. Gonzalez, S. Ghostine, and C. Caussin, "Optical coherence tomography: From physical principles to clinical applications," *Archives of Cardiovascular Diseases*, vol. 105, no. 10, pp. 529–534, Oct. 2012. [Online]. Available: https://www.sciencedirect.com/science/article/pii/S1875213612001490

[31] J. Liu, "Optimization of Multi-Functional 1310 nm Spectral-Domain Optical Coherence Tomography (SD-OCT) System and Three-Dimensional Volumetric OCT Image Registration," Ph.D. dissertation, UC Riverside, 2017. [Online]. Available: https://escholarship.org/uc/item/0hb3r0tg

[32] B. George, "Swept-Frequency Sampled Grating Distributed Bragg Reflector Lasers Optimized for Optical Coherence Tomography Applications," *Master's Theses*, Dec. 2009. [Online]. Available: https://digitalcommons.calpoly.edu/theses/220

[33] Y. Ma, X. Chen, W. Zhu, X. Cheng, D. Xiang, and F. Shi, "Speckle noise reduction in optical coherence tomography images based on edge-sensitive cGAN," *Biomedical Optics Express*, vol. 9, no. 11, pp. 5129–5146, Oct. 2018. [Online]. Available: https://www.ncbi.nlm.nih.gov/pmc/articles/PMC6238896/

[34] S. Liu, A. S. Paranjape, B. Elmaanaoui, J. Dewelle, H. G. Rylander, M. K. Markey, and T. E. Milner, "Quality assessment for spectral domain optical coherence tomography (OCT) images," *Proceedings of SPIE*, vol. 7171, p. 71710X, 2009. [Online]. Available: https://www.ncbi.nlm.nih.gov/pmc/articles/PMC2860632/

[35] M. Pircher, E. Götzinger, R. A. Leitgeb, A. F. Fercher, and C. K. Hitzenberger, "Speckle reduction in optical coherence tomography by frequency compounding," *Journal of Biomedical Optics*, vol. 8, no. 3, pp. 565–569, Jul. 2003. [Online]. Available: https://www.spiedigitallibrary.org/journals/journal-of-biomedical-optics/volume-8/issue-3/0000/Speckle-reduction-in-optical-coherence-tomography-by-frequency-compounding/10.1117/1.1578087.full

[36] F. N. Rahatabad and E. F. Bahalgerdy, "Speckle Noise Reduction for the Enhancement of Retinal Layers in Optical Coherence Tomography Images," 2015.

[37] O. Miljković, "Image pre-processing tool," *Kragujevac Journal of Mathematics*, vol. 32, no. 32, pp. 97–107, 2009. [Online]. Available: https://eudml.org/doc/252610

[38] M. Sonka, V. Hlavac, and R. Boyle, "Image pre-processing," in *Image Processing, Analysis and Machine Vision*, M. Sonka, V. Hlavac, and R. Boyle, Eds. Boston, MA: Springer US, 1993, pp. 56–111. [Online]. Available: https://doi.org/10.1007/978-1-4899-3216-7_4

[39] I. T. Young, J. J. Gerbrands, L. J. van Vliet, and F. d. T. N. TU Delft, *Fundamentals of Image Processing: [Dictaat Behorende Bij College Et2720in*. Delft: Delft University of Technology, 1998.

[40] "Morphological Image Processing." [Online]. Available: https://www.cs.auckland.ac.nz/courses/compsci773s1c/lectures/ImageProcessing-html/topic4.htm

[41] S. Krig, *Computer Vision Metrics : Survey, Taxonomy, and Analysis*. Springer Nature, 2014. [Online]. Available: https://library.oapen.org/handle/20.500.12657/28173

[42] "Types of Morphological Operations - MATLAB & Simulink." [Online]. Available: https://www.mathworks.com/help/images/morphological-dilation-and-erosion.html

[43] M. R and M. R, "A methodical review on image stitching and video stitching techniques," *International Journal of Applied Engineering Research*, vol. 11, no. 5, pp. 3442–3448, Jan. 2016. [Online]. Available: https://research.vit.ac.in/publication/a-methodical-review-on-image-stitching-and-video-stitching

[44] E. Adel, E. Elbasyouny, M. Hazem, H. El-Bakry, and M. Mahfouz, "A Proposed System for Automatic Panoramic Image Stitching," Ph.D. dissertation, Mar. 2019.

[45] L. M. G. Fonseca and B. S. Manjunath, "Registration Techniques for Multisensor Remotely Sensed Images," Photogrammetric Engineering," *and Remote Sensing*, pp. 1049–1056, 1996.

[46] "Image registration methods: A survey - ScienceDirect." [Online]. Available: https://www.sciencedirect.com/science/article/abs/pii/S0262885603001379

[47] P. Khanna, "Harris Corner Detector-an Overview of the Original Paper," Nov. 2019. [Online]. Available: https://medium.com/swlh/harris-corner-detector-an-overview-of-the-original-paper-cf20c502ab0f

[48] D. G. Lowe, "Distinctive Image Features from Scale-Invariant Keypoints," *International Journal of Computer Vision*, vol. 60, no. 2, pp. 91–110, Nov. 2004. [Online]. Available: http://link.springer.com/10.1023/B:VISI.0000029664.99615.94

[49] H. Bay, T. Tuytelaars, and L. Van Gool, "SURF: Speeded Up Robust Features," in *Computer Vision – ECCV 2006*, ser. Lecture Notes in Computer Science, A. Leonardis, H. Bischof, and A. Pinz, Eds. Berlin, Heidelberg: Springer, 2006, pp. 404–417.

[50] E. Rublee, V. Rabaud, K. Konolige, and G. Bradski, "ORB: An efficient alternative to SIFT or SURF," in *2011 International Conference on Computer Vision*. Barcelona, Spain: IEEE, Nov. 2011, pp. 2564–2571. [Online]. Available: http://ieeexplore.ieee.org/document/6126544/

[51] "Parallel processing for adaptive optics optical coherence tomography (AO-OCT) image registration using GPU | Semantic Scholar." [Online]. Available: https://www.semanticscholar.org/paper/Parallel-processing-for-adaptive-optics-optical-GPU-Do/b4877cafb2fbae8df26b1dbd2665107fcb02d600

[52] Z. Yang, "Fast Template Matching Based on Normalized Cross Correlation with Centroid Bounding," in *2010 International Conference on Measuring Technology and Mechatronics Automation*, vol. 2, Mar. 2010, pp. 224–227.

[53] "High Resolution Wide Field-of-View Optical Coherence Tomography For 3D Imaging - University of Miami." [Online]. Available: https://scholarship.miami.edu/esploro/outputs/doctoral/High-Resolution-Wide-Field-of-View-Optical-Coherence-Tomography-For-3D-Imaging/991031447768802976

[54] L. Zhang, T. Wen, and J. Shi, "Deep Image Blending," *arXiv:1910.11495 [cs]*, Oct. 2019. [Online]. Available: http://arxiv.org/abs/1910.11495

[55] V. Rankov, R. Locke, R. Edens, P. Barber, and B. Vojnovic, "Title>An Algorithm for image stitching and blending," *Carol J. Cogswell*, vol. 5701, Mar. 2005.

[56] V. A. Robles, "Automated image analysis of corneal structures in anterior-segment optical coherence tomography and in-vivo confocal microscopy images," Doctor of Philosophy, University of Iowa, Dec. 2017. [Online]. Available: https://iro.uiowa.edu/discovery/fulldisplay/alma9983777288202771/01IOWA_INST:ResearchRepository

[57] "Thorlabs - CR1/M-Z7 Motorized Continuous Rotation Stage, Metric." [Online]. Available: https://www.thorlabs.com/thorproduct.cfm?partnumber=CR1/M-Z7

[58] "IRB 1200 | ABB Robotics." [Online]. Available: https://new.abb.com/products/robotics/industrial-robots/irb-1200

[59] "Noetic - ROS Wiki." [Online]. Available: http://wiki.ros.org/noetic

[60] "ROS/Concepts - ROS Wiki." [Online]. Available: http://wiki.ros.org/ROS/Concepts

[61] Y. Gan, "Image analytic tools for tissue characterization using optical coherence tomography," Ph.D. dissertation, Columbia University, 2017. [Online]. Available: https://doi.org/10.7916/D8VM4HXT

[62] F. Jin, P. Fieguth, L. Winger, and E. Jernigan, "Adaptive Wiener filtering of noisy images and image sequences," in *Proceedings 2003 International Conference on Image Processing (Cat. No.03CH37429)*, vol. 3, Sep. 2003, pp. III–349.

[63] K. Dabov, R. Foi, V. Katkovnik, and K. Egiazarian, "Image denoising with block-matching and 3d filtering," in *In Proc. SPIE Electronic Imaging*, 2006.